Ore genesis of the Fule Pb-Zn deposit and its relationship with the Emeishan Large Igneous Province: Evidence from mineralogy, bulk C-O-S and in situ S-Pb isotopes

Jia-Xi Zhou[a, c, f, *], Kai Luo[a, b], Xuan-Ce Wang[c], Simon A. Wilde[c], Tao Wu[d, f], Zhi-Long Huang[a], Yin-Liang Cui[e], Jian-Xin Zhao[f]

[*]Corresponding author, E-mail, zhoujiaxi@vip.gyig.ac.cn

[a] *Stake Key Laboratory of Ore Deposit Geochemistry, Institute of Geochemistry, Chinese Academy Sciences, Guiyang 550081, China*

[b] *University of Chinese Academy Sciences, Beijing 100049, China*

[c] *The Institute for Geoscience Research, Department of Applied Geology, Curtin University, GPO Box U1987, Perth WA 6845, Australia*

[d] *School of Earth Sciences, Zhejiang University, Hangzhou 310027, China*

[e] *Yunnan Nonferrous Metals Geological Bureau, Kunming 650051, China*

[f] *Radiogenic Isotope Facility, School of Earth and Environment Sciences, University of Queensland, Brisbane QLD 4072, Australia*

ABSTRACT

Magmatic activity plays an important role in mineralization, but little is understood of its role with respect to carbonate-hosted stratabound epigenetic Pb-Zn deposits. The Fule Pb-Zn deposit (~10 Mt of sulfide ore with mean grades of 15-20 wt. % Zn + Pb), is stratigraphically placed in middle Permian strata and spatially (~1 m) associated with late Permian continental flood basalts of the Emeishan Large Igneous Province (ELIP). It thus provides an ideal case to investigate its genetic relationship with the ELIP. In addition, the Fule deposit is characterized by high concentrations of Ag, Cd, Ge and Ga, and contains a variety of Cu and Ni sulfide minerals. Syn-ore calcite ($\delta^{13}C$ = +2.57-+3.01‰) and associated fluids ($\delta^{13}C$ = +2.96-+3.40‰) have $\delta^{13}C$ values similar to those of fresh limestone ($\delta^{13}C$ = +1.58-+2.63‰), but the $\delta^{18}O$ values of calcite (+16.83-+19.92‰) and associated fluids (+7.80-+10.89‰) are distinctly lower than those of limestone ($\delta^{18}O$ = +21.85-+23.61‰). This means that C is mainly derived from limestone, whereas the O isotope signature may be related to water/rock (W/R) interaction between mantle and/or metamorphic fluids and limestone. $\delta^{34}S$ values of sulfide minerals obtained by in situ NanoSIMS and conventional bulk techniques record a range of +9.8-+23.1‰ and +10.04-+16.43‰, respectively, reflecting the enrichment of heavy S isotopes in the ore-forming fluids and thermochemical sulfate reduction (TSR) is the principal mechanism for the formation of S^{2-}. Cores of sulfide crystals have much higher $\delta^{34}S$ values than their rims, indicating a probable mixture of multiple S reservoirs and/or a dynamic fractionation of S isotopes occurred during sulfide precipitation. The uniform femtosecond (fs) LA-MC-ICPMS in situ Pb isotopic data for galena plot in the field that differs from any of the three potential

sources in the region. Such signatures demonstrate that metal Pb was most likely derived from a well-mixed source of basalts, sedimentary rocks and basement rocks. We propose that (a) the enrichment in Ag, Cu, Ni, Cd, Ge and Ga, and the isotope signatures of hydrothermal minerals in the Fule region are related to fluids derived from or flowed through multiple reservoirs; (b) Emeishan magmatism provided heat, elements and associated fluids, and its basalts acted as an impermeable and protective layer; and (c) fluid mixing caused TSR, and then resulted in W/R interaction and CO_2 degassing, all of which played a key role in the precipitation of hydrothermal minerals.

Key words NanoSIMS in situ S isotopes; Fs LA-MC-ICPMS in situ Pb isotopes; Role of Emeishan magmatism; Carbonate-hosted Pb-Zn deposits in the ELIP, South China

1. Introduction

Carbonate-hosted stratabound epigenetic Pb-Zn deposits, traditionally named as Mississippi Valley-type (MVT), are an important source of base metal ores that form in sediments some time during the lifetime of a sedimentary basin (Anderson and Macqueen, 1982). MVT deposits predominantly form in platform carbonate sequences and are typically located within extensional zones inboard of orogenic belts (Leach et al., 2005). As such type of deposits is characterized by the absence of temporally or spatially associated magmatic activity, the classical thinking about the origin of MVT deposits is that it was related to the low temperature (50-200 °C) and high salinity (10-30 wt. % NaCl equiv.) basin brines (Leach et al., 2010). However, many carbonate-hosted Pb-

Zn deposits are spatially associated with igneous rocks, but whether they are related to the igneous activity is unclear and needs to be carefully investigated. In the western Yangtze Block (Fig. 1a), South China, there are more than 400 carbonate-hosted Pb-Zn deposits and many basalt-hosted native Cu deposits within the Emeishan Large Igneous Province (ELIP) (Fig. 1b) (Liu and Lin, 1999; Zhu et al., 2007; Zhou et al., 2014a). These Pb-Zn deposits form the giant Sichuan-Yunnan-Guizhou (SYG) Pb-Zn metallogenic province (Fig. 1a-b), representing ~27% of the total Zn + Pb resources in China, and are an important part of the South China low-temperature metallogenic domain (Zhou et al., 2013a; Wang et al., 2014; Zhang et al., 2015; Hu et al., 2017). The SYG province is structurally bounded by the N-S-trending Anninghe-Lvzhijiang, the NE-SW-trending Mile-Shizong-Shuicheng and the NW-SE-trending Kangding-Yiliang-Shuicheng (Fig. 1a) faults. The Pb-Zn deposits in the SYG province are characterized by (a) ore bodies that are hosted by late Ediacaran to middle Permian carbonate rocks that are spatially associated with late Permian Emeishan continental flood basalts (Figs. 1b, 2-3); (b) ore bodies that have stratiform or lentiform shape within bedding-planes and/or steeply-dipping veins along fault dip planes (Zheng and Wang, 1991; Li et al., 2007; Zhou et al., 2013b; Wei et al., 2015; Jin et al., 2016; Zhu et al., 2016); (c) sulfide ore that has high mean grades of 10-35 wt. % Zn + Pb, and high contents of Ag, Cu, Cd, Ge and Ga (Si et al., 2006; Ye et al., 2011; Zhou et al., 2011, 2014b; Zhu et al., 2017); and (d) ore-forming fluids of low-medium temperatures (<300 °C) and salinities (<15 wt. % NaCl equiv.) (Bai et al., 2013; Li et al., 2015; Zhang et al., 2015; Liu et al., 2017). These features are significantly different from those of typical MVT deposits (Leach et al., 2005, 2010). As the only large-scale igneous event

between the Ediacaran and Triassic in the SYG province was eruption of the Emeishan flood basalts, the above mineralization features were generally considered to be related to the ELIP (Huang et al., 2010; Xu et al., 2014; Zhou et al., 2013a, 2014a; Li et al., 2016).

The Fule Pb-Zn deposit, hosted by carbonate rocks of the middle Permian Yangxin Formation (Si et al., 2006), is stratigraphically and spatially (~1 m) close to the late Permian Emeishan basalts (Figs. 1b, 2-3). This deposit contains very high ore grades (up to 60 wt. % Zn + Pb, mean 15-20 wt. %) and is rich in multiple elements (4567 t Cd, 329 t Ge, and 177 t Ga at mean grades of 0.127 wt. % Cd, 0.012 wt. % Ge, and 0.007 wt. % Ga) (Si et al., 2011, 2013; Ye et al., 2011). These features are similar to those of the adjacent world-class Huize Pb-Zn deposit (hosted in Carboniferous strata with >30 Mt of sulfide ore with average grades of 25-35 wt. % Zn + Pb) (Fig. 1b) (Zhou et al., 2001; Li et al., 2006; Huang et al., 2010; Bao et al., 2017), which is considered to be a typical representative of the unique SYG-type deposits (related to the ELIP) in the western Yangtze Block (Huang et al., 2010). In spite of this, there is still debate on the ore genesis type, including whether it is a distal magmatic hydrothermal-type (based on geological evidence: Liu and Lin, 1999), stratabound-type (based on trace element data: Si et al., 2006, 2011) or MVT (based on Cd isotopic data: Zhu et al., 2017). Hence, the Fule deposit provides an ideal case for understanding the role of magmatism during the formation of carbonate-hosted Pb-Zn deposits.

Micro-scale variation of elements and isotopes in hydrothermal minerals, obtained by micro-beam analysis, can provide crucial clues for revealing the source and evolution of ore-forming elements and associated fluids, and the

cause of hydrothermal mineral precipitation (Barker et al., 2009; Nishizawa et al., 2010; Ye et al., 2011; Jin et al., 2016; Deng et al., 2017). Laser-ablation multi-collector inductively coupled plasma mass spectroscopy (LA-MC-ICPMS) and secondary ion mass spectroscopy (SIMS) can accurately analyze isotopic compositions of hydrothermal minerals in situ (Ikehata et al., 2008; Zhang et al., 2014; Yuan et al., 2015; Bao et al., 2016). Here we use the Fule deposit as a case study, utilizing NanoSIMS in situ S, femtosecond (fs) LA-MC-ICPMS in situ Pb, and bulk C-O-S isotope analyses, together with a detailed dataset of the ore deposit geology and mineralogy, aimed at revealing the ore genesis of the Fule deposit and its relationship with the ELIP. The outcomes will have wide significance for further exploration of carbonate-hosted Pb-Zn deposits in the ELIP and can open the door to similar situations in other Large Igneous Provinces where they interact with carbonate rocks.

2. Geological setting

2.1 Geology of the western Yangtze Block

The Yangtze Block is bounded by the Cathysia Block to the southeast, the Sanjiang Orogenic Belt to the southwest and the Songpan-Ganzê Orogenic Belt to the northwest (Fig. 1a). In the western Yangtze Block, the basement is comprised of late Paleoproterozoic to early Neoproterozoic metamorphic rocks, which were intruded by late Neoproterozoic and Mesozoic igneous rocks (Fig. 1b) (Gao et al., 2011; Zhou et al., 2014c; Hu et al., 2017). The cover sequence in the western Yangtze Block is late Ediacaran to Triassic marine, and Jurassic to Cenozoic continental sedimentary rocks (Liu and Lin, 1999; Yan et al., 2003;

Zhou et al., 2013a). The platform carbonate sequences constitute an important part of the late Ediacaran to Triassic marine strata, which are rich in salt-gypsum and organic matters (Huang et al., 2004; Jin, 2008; Zhou et al., 2014a). The western margin of the Yangtze Block is characterized by multiple processes of tectonic activity, which strictly controlled sedimentation, magmatism and mineralization (Figs. 1b, 2).

The late Permian ELIP (263-259 Ma) covers ~0.3×10^6 km^2 of the western Yangtze Block and eastern Songpan-Ganzê Orogenic Belt (Fig. 1a-b), with displaced correlative units in northern Vietnam (Song Da zone). It hosts many economically important Fe-Ti-V oxide deposits, Ni-Cu-(PGE) sulfide deposits and native Cu deposits (Zhou et al., 2002; Ali et al., 2005; Zhu et al., 2007; Jian et al., 2009; Shellnutt, 2014; Tran et al., 2016). The Emeishan flood basalts constitute a significant part of the ELIP, and are up to ~5 km maximum thickness in the western part of the ELIP (i.e. Yunnan), whereas the maximum thickness is only a few hundred meters in the eastern part (i.e. Guizhou) (Xu et al., 2001; Pirajno, 2013; Shellnutt, 2014). After eruption of the Emeishan basalts, the Indosinian Orogeny (257-200 Ma) resulted from closure of Paleotethys (Carter et al., 2001; Lepvrier et al., 2004; Enkelmann et al., 2007; Reid et al., 2007; Pullen et al., 2008; Qiu et al., 2016), resulting in faulting and folding that structurally controlled the occurrence of hydrothermal deposits in the western Yangtze Block (Fig. 1b) (Liu and Lin, 1999; Zaw et al., 2007; Zhu et al., 2007; Hu and Zhou, 2012; Chen et al., 2015).

The SYG Pb-Zn metallogenic province covers ~0.2×10^6 km^2 of SW Sichuan, NE Yunnan and NW Guizhou provinces (Fig. 1a), and hosts 408 carbonate-hosted Pb-Zn deposits in late Mesoproterozoic to late Paleozoic, all of which are spatially associated with the late Permian Emeishan basalts (Fig. 1b) (Liu and Lin, 1999; Zhou et al., 2013a; Wang et al., 2014; Zhang et al., 2015; Hu et al., 2017). These deposits were formed between 245 Ma and 192±7 Ma as constrained by Pb model ages, and hydrothermal calcite/fluorite Sm-Nd and sphalerite/pyrite Rb-Sr isochron dating (Guan and Li, 1999; Si et al., 2006; Li et al., 2007; Lin et al., 2010; Mao et al., 2012; Zhou et al., 2013a, 2013b, 2015; Zhang et al., 2015). These dates broadly match the ages of basalt-hosted native Cu deposits in the ELIP (231±3-225±2 Ma: Zhu et al., 2007), Carlin-like Au deposits in the Youjiang Basin (235±33-204±19 Ma: Chen et al., 2015) and detritus (~230-206 Ma) in the Songpan-Ganzê Orogenic Belt that resulted from collision with the western Yangtze Block during the late Triassic (Enkelmann et al., 2007).

2.2 Regional geology of the Fule district

The Fule carbonate-hosted Pb-Zn deposit is located 110 km NE of Luoping City, NE Yunnan Province (Fig. 1b). The exposed rocks include the Mesoproterozoic Kunyang Group basement rocks, and late Paleozoic (middle Devonian, Carboniferous and Permian) and early Mesozoic (early-middle Triassic) cover sequences (Si et al., 2006; Lu et al., 2015). The Kunyang Group is composed mainly of mudstone and metasandstone, which are unconformably overlain by

194 the middle Devonian Haikou Formation that consists mainly of limestone and
195 sandstone. The Haikou Formation sedimentary rocks are unconformably
196 overlain by early Carboniferous coal-bearing clastic rocks and late
197 Carboniferous carbonate rocks. Sedimentary rocks of Carboniferous age are
198 conformably overlain by early Permian limestone, shale and sandstone, which
199 are in turn conformably overlain by limestone and dolostone of middle Permian
200 Yangxin Formation. Carbonate rocks of the Yangxin Formation are
201 disconformably overlain by late Permian, which consists mainly of Emeishan
202 basalts, and coal-bearing clastic rocks. Late Permian clastic rocks are
203 conformably overlain by early Triassic sandstone, mudstone and carbonates,
204 which are in turn overlain conformably by middle Triassic carbonates.
205 The Mile-Shizong-Shuicheng fault (Fig. 1a) and Faben anticline (Si et al., 2011;
206 Lu et al., 2015) form major structural features in the studied district. The Mile-
207 Shizong-Shuicheng regional fault strikes NE-SW, with a slight bend in the Fule
208 district (Fig. 1b). It consists of a series of secondary fractures that controlled the
209 distribution of Pb-Zn deposits (Figs. 2-3) (Liu and Lin, 1999; Zhou et al., 2013b;
210 Qiu et al., 2016). The Faben anticline is 20 km in length and 10 km wide, and
211 is a gentle fold structure whose axis strikes 030-040° (Si et al., 2006).
212 Carboniferous rocks in the central part of the anticline have a horizontal dip
213 angle, whereas Permian rocks dip at 5°-10°. The Emeishan flood basalts are
214 widely distributed in the Fule district, but their thickness is relatively thin, as they
215 form the southeastern margin of the ELIP (Liu and Lin, 1999; Xu et al., 2001;

Pirajno, 2013; Shellnutt, 2014).

More than 10 Pb-Zn ore deposits have been discovered over ~60 km^2 in the Fule district (Fig. 2), including the Fule (~10 Mt of sulfide ore with mean grades of 15-20 wt. % Zn + Pb), Fusheng (~3 Mt of sulfide ore with average grades of 15-25 wt. % Zn + Pb) and Fuli (~1 Mt of sulfide ore with mean grades of 10-15 wt. % Zn + Pb) deposits (Si et al., 2006; Lu et al., 2015). All the Pb-Zn deposits are hosted by carbonate rocks of the middle Permian Yangxin Formation (Figs. 2-3). Ore bodies occur as stratiform or lentiform shapes along bedding-planes (Fig. 3), and are structurally controlled by the regional fault-fold system (Figs. 1b, 2-3). A principal feature of these deposits is that they are rich in Ag, Cu, Cd, Ge and Ga (Si et al., 2006; Ye et al., 2011; Zhu et al., 2017).

3. Geology of the Fule ore deposit

3.1 Stratigraphy and lithology

In the Fule mining area, the exposed lithologies include Permian, early-middle Triassic and Quaternary rocks (Figs. 2-3). The late Carboniferous Maping Formation was exposed by underground mining tunnels (Fig. 3), and consists mainly of dolomitic bioclastic limestone. The Maping Formation limestone is conformably overlain by the early Permian Liangshan Formation that is mainly composed of limestone, shale and sandstone. Sedimentary rocks of the Liangshan Formation are conformably overlain by carbonate rocks of the middle Permian Yangxin Formation, which are in turn disconformably overlain

238 by late Permian Emeishan flood basalts. The basalts are disconformably
239 overlain by the terrestrial coal-bearing clastic sequence of the late Permian
240 Xuanwei Formation. Clastic rocks of the Xuanwei Formation are conformably
241 overlain by the early Triassic Feixianguan Formation, which consists mainly of
242 sandstone, shale and argillaceous limestone. The Feixianguan Formation
243 sedimentary rocks are conformably overlain by the early Triassic Yongzhenning
244 Formation that is composed mainly of carbonate rocks, which are in turn
245 conformably overlain by oolitic dolostone and limestone of the middle Triassic
246 Guanling Formation. Quaternary sediments locally overlie the Permian and
247 Triassic rocks (Figs. 2-3).

248 ***3.2 Structural Geology***

249 The major structures in the Fule mining area include secondary structures of
250 the Mile-Shizong-Shuicheng regional fault and the right limb of the Faben
251 anticline (Figs. 1b, and see Figs. 2-3 for the details). The F_4 fault is a normal
252 structure and strikes 000°-030° with a length of 43 km (Figs. 2-3). The F_5 fault
253 is a reverse fault and trends 000-045° and is 17 km long (Figs. 2-3). Another
254 important fault, the F_6 reverse fault (Fig. 4a), is 20 km in length and strikes 000-
255 050° (Figs. 2-3). The F_5 and F_6 reverse faults controlled the occurrence of the
256 Pb-Zn ore bodies in the Fule mining area (Figs. 2-3).

257 ***3.3 Magmatic rocks***

258 The Emeishan flood basalts are the only igneous rocks exposed in the Fule
259 mining area, and have a close spatial association with all the known Pb-Zn

deposits (Figs. 2-3). The distance between the basalts and Pb-Zn ores is less than 1 m locally (Fig. 3).

3.4 Ore bodies

Twenty-ore bodies have been discovered in the Fule deposit, all of which are buried, and these have a total NW-SE length of 3000 m and NE-SW width of 1500 m. They have been divided into the Laojuntai and Xinjuntai sections, with the Laojuntai section having been completely mined-out (Si et al., 2011). Ore bodies in the Xinjuntai section occur as stratiform to lentiform shapes or as veins along bedding-planes within the Yangxin Formation; they trend SE with a dip of 10° (Fig. 3). The Erdong stratiform ore body is the largest one in the Xinjuntai section, and is 1000 m in length, 300-500 m in width and 0-20 m in thickness. The next largest is the Danaotang ore body, which is lenticular and 500 m long, 400 m wide and 0-20m thick. These large ore bodies have also been completely mined-out. The total mined-out sulfide ore in the two sections are more than 7 Mt (Si et al., 2013). Some medium-scale ore bodies have been found recently, for example, the No. 108 stratiform ore body, which is 400 m long, 200m wide and 2-12 m thick; the No. 904 lentiform ore body, which is 340 m in length, 200m in width and 1.5-15m in thickness; and the No.74 veined ore body, which is 200 m long, 150 m wide and 3-15 m thick. Sulfide ore in these newly-discovered ore bodies contains Zn + Pb grades up to 60 wt. %, averaging 15-20 wt. %, and 256-8171 μg/g Cd, 1.77-239 μg/g Ge, 0.74-182 μg/g Ga, 23.5-107 μg/g Se, and 0.98-122.1 g/t Ag. The total metal reserves of Cd, Ge and Ga

are more than 4567 t, 329 t and 177 t, respectively (Si et al., 2006, 2011, 2013; Zhu et al., 2017).

3.5 Structure and texture of the sulfide ores

Previous studies showed that sulfide ore in the Fule deposit is composed mainly of sphalerite, galena and pyrite, with calcite and dolomite as gangue minerals (Figs. 4-7). In this study, Cu and Ni sulfide minerals, together with apatite (Fig. 7f), have been identified, including tetrahedrite (Figs. 6g, k, m, t and 7g-h, j, l-s), chalcopyrite (Fig. 6i, r-t), millerite, polydymite, and pentlandite (Fig. 7s).

The main sulfide minerals occur as either massive (Figs. 4c-f, h-o, q-s and 5a, e, k-q), veined (Figs. 4h, 5b-d, i-j, r-t and 6a-c), disseminated (Figs. 4p and 5g-h, n, r-s) or brecciated (Figs. 4g, 5f and 6d) structure. Aggregations of sulfide minerals in the wall rocks form massive ore (Figs. 4c-e, i-j, n-o and 5a, k); sulfide veins between millimeter-scale veinlets (Figs. 4h, 5b-d and 6a) or centimeter-scale veins of calcite/dolomite (Figs. 5i-j, r-t and 6b-c) constitute the veined ore, whereas in the disseminated ore, sulfide minerals occur as speckles or single crystals irregularly distributed in the wall rocks (Fig. 4p) or in calcite/dolomite veins (Fig. 5g-i, n, r-s). In the brecciated ore, fragments of sulfides and carbonate rocks are enclosed in calcite/dolomite cements (Figs. 4g and 5f).

The hydrothermal minerals occur in a variety of forms and may be granular (Figs. 6e-t and 7a-t), form replacement minerals (Fig. 6r), have embayments (Figs. 6f, l, s and 7b, d, j, m), occur in solid-solution (Figs. 6i, s and 7a-b, d, k, o, s), show stress deformation (Figs. 6e-f, l-m and 7g-h) or have cataclastic

304 textures (Fig. 6n). Granular form is common and sphalerite occurs as euhedral
305 to anhedral fine- (< 0.5 mm, Figs. 6e-f, h, j-m, o-r, t and 7a, c, h-i, p), medium-
306 (0.5-5 mm, Fig. 6g, k-l and 7a-d, q) to coarse-grained minerals (> 5 mm, Figs.
307 5i, n, r-s, 6b-d, i, s and 7t); Galena is euhedral to anhedral, fine- to coarse-
308 grained with grain sizes of 0.01-15 mm (Figs. 5k, 6c, e-f, l-m and 7a-h, j, i-t).
309 Stress deformation is a common feature in galena (Figs. 6e-f, l-m and 7g-h).
310 Chalcopyrite has a solid-solution texture within sphalerite (Fig. 6i, s) or else
311 replaces pyrite (Fig. 6r). The contacts between sphalerite and galena (Fig. 6f, l)
312 or calcite/dolomite (Fig. 6s and 7b, d, j, m) commonly show embayment. Pyrite
313 has commonly has a cataclastic texture (Figs. 6h, n and 12). In contrast,
314 millerite and pentlandite occur as a solid-solution in polydymite (Fig. 7s),
315 whereas calcite and dolomite often form solid-solutions (Fig. 7a-b, d, k, o, s).

316 ***3.6 Mineral paragenesis***

317 Based on macro-scale geological observations, microscope identification and
318 scanning electron microscopy (SEM) analysis, together with previously
319 published geological data (Si et al., 2006, 2011), the ore-forming process of the
320 Fule deposit can be divided into diagenetic, hydrothermal and supergene
321 periods (Fig. 8). The hydrothermal period can be further divided into sulfide +
322 carbonate (including two generations, i.e. I and II) and barren carbonate
323 (includes one generation, namely III) stages (Fig. 8). There are two principal
324 sulfide ore types: sphalerite-dominated (Figs. 4h, q, 5a-j, p-t and 6a-c) and
325 sphalerite + galena-dominated (Figs. 4c-f, i-p, r-s, 5k-o and 6d). These two ore

types have the following spatial distribution from bottom to top as follows: massive sphalerite-dominated ore often occurs at the bottom of the ore body (Fig. 4j, m, o, q), followed by massive sphalerite + galena-dominated (Figs. 4c-f, i-p, r-s and 5n) or sphalerite-dominated interbedded veins (Figs. 4h, 5b-d, i-j, r-t and 6a-c), with disseminated sphalerite + galena-dominated ore commonly at the top (Figs. 4p and 5g-j, n, r-s).

Overall, there are at least two generations of hydrothermal minerals formed in the two types of sulfide ore. Sphalerite-I is euhedral (Figs. 5e, h, j, o, r and 6i) to anhedral (Figs. 5f-g, k-n and 6a-e) fine- to medium-grained (0.01-0.5 mm), coexisting with galena-I (Figs. 6a-c and 7a, q), pyrite-I (Figs. 6k, 7e and 10), tetrahedrite (Figs. 6m and 7h, q) or calcite/dolomite-I (Figs. 6a-c and 7a-b), and is enclosed by galena-II (Figs. 6f, l-m and 7h, l), as well as being filled by galena-II (Fig. 6g, q and 7g, t), tetrahedrite (Figs. 6h and 7g), pyrite-II (Fig. 6n), calcite/dolomite-II (Figs. 6g, k, n, q and 7a, e) or replaced by chalcopyrite (Fig. 6i). Sphalerite-II occurs as subhedral to anhedral medium- to coarse-grained crystals (0.5-10 mm) that coexist with galena-II (Figs. 6e-f, l, p, r and 7h, j, l, p, r), pyrite-II (Figs. 6h, r and 7c-d), tetrahedrite (Fig. 6t and 7l, p, r), chalcopyrite (Fig. 6r) or calcite/dolomite-II (Fig. 6e-f, p, s-t), and are enclosed by calcite/dolomite-II (Figs. 6h, j, o, r and 7i). Galena-I is euhedral to anhedral fine- to medium-grained (0.01-0.1 mm), and coexists with sphalerite-I (Figs. 6a-c and 7a, q), pyrite-I (Fig. 7e) or calcite/dolomite-I (Figs. 6a-c and 7a), and is enclosed by pyrite-II (Fig. 7c-d) or calcite/dolomite-II (Fig. 7e, m, o). Galena-II forms

subhedral to anhedral medium- to coarse-grained crystals (0.1-15 mm) that coexist with sphalerite-II (Figs. 6e-f, l, p, r and 7h, j, l, p, r), tetrahedrite (Figs. 6g and 7l-m, o-p), or calcite/dolomite-II (Figs. 6e-g, p-r and 7m-o), and enclose sphalerite-I (Figs. 6f, l-m and 7h, l), pyrite-I (Figs. 6r and 7n) or tetrahedrite (Figs. 6m and 7h, j, n, r), as well as filling sphalerite-I (Figs. 6g, q and 7g, t). Pyrite-I coexists with sphalerite-I (Figs. 6k, 7e and 11) or galena-I (Fig. 7e), and is enclosed by galena-II (Figs. 6r, and 7n) or calcite/dolomite-II (Fig. 7e). Pyrite-II coexists with sphalerite-II (Figs. 6h, r and 7c-d) or calcite/dolomite-II (Figs. 6h, n, r and 7c-d), and encloses galena-I (Fig. 7c-d), as well as being replaced by chalcopyrite (Fig. 6r). Syn-ore calcite/dolomite-I occurs as crumbs or millimeter-scale discrete veinlets that enclose or coexist with sphalerite-I and galena-I (Figs. 6a-c and 7a-b). Syn-ore calcite/dolomite-II forms centimeter-scale veins (Figs. 5i-j, r-t and 6b-d) that fill, cement or coexist with two generations of sulfide minerals (Figs. 6-7). Post-ore calcite/dolomite-III occurs as veinlets or stockworks that fill fractures in the sulfide ores (Figs. 4e-g and 6a) or cement carbonate breccias (Fig. 4b, t). In addition, millerite and pentlandite coexists with galena-I and all are enclosed by polydymite (Fig. 7s). Apatite occurs as euhedral crystal and is enclosed by dolomite-III that fills fractures in galena-II (Fig. 7f).

3.7 Wall rock alteration

Wall rock alteration includes chloritization and carbonatization, which can be divided into pre- and post-ore stages. The pre-ore stage of chloritization

generated chlorite along fault planes within the basalts (Fig. 4a), and carbonatization recrystallized coarse-granular dolostone (Fig. 4b-c). The post-ore stage is of carbonatization forming barren carbonate (dolomite and calcite) veins or veinlets, which cement/fill fractures within sulfide ore (Figs. 4e-g and 6a) or wall rocks (Fig. 4b, t). The pre-ore chloritization/carbonatization, resulted from water/rock interaction between fluids and basalts/carbonates, usually occur along fluid migration pathways. The post-ore alteration is always close to sulfide ore, and thus can be used as a clue in mineral exploration.

4. Samples and analytical methods

4.1 Samples

Sulfide ore samples were collected mainly from the newly-discovered ore bodies, because the other main ore bodies had been mined-out completely (Si et al., 2011). Seven calcite and ten sulfide mineral separates were handpicked from seventeen sulfide ore samples, which were used for bulk C-O and S isotope analyses, respectively. Four fresh limestone samples were also used for bulk C-O isotope analysis. Twelve polished thin sections of sulfide ores were used for NanoSIMS in situ S and Fs-LA-MC-ICPMS in situ Pb isotope analyses. In situ $\delta^{34}S$ values for galena were not obtained, because no galena standard was available (Tang et al., 2014; Zhang et al., 2014). Also, no in situ Pb isotopic ratios of pyrite and sphalerite were obtained as their high Hg contents could markedly affect the quality of the data (Chen et al., 2014; Bao et al., 2016, 2017;

392 Tan et al., 2017).

393 ***4.2 Analytical methods***

394 *4.2.1 Bulk C-O isotope analysis*

395 Bulk C-O isotope analysis was performed at the State Key Laboratory of Ore
396 Deposit Geochemistry (SKLODG), Institute of Geochemistry (IG), Chinese
397 Academy Sciences (CAS), using a Finnigan MAT-253 mass spectrometer.
398 Calcite separates and limestone whole-rock reacted with 100% H_3PO_4 to
399 produce CO_2. The analytical precisions calculated from replicate analyses of
400 unknown samples were better than 0.2‰ (2σ) and 1‰ (2σ) for $\delta^{13}C$ and $\delta^{18}O$,
401 respectively. The $\delta^{13}C$ and $\delta^{18}O$ values were reported relative to the Vienna
402 Pee Dee Belemnite (V-PDB) standard and Standard Mean Ocean Water
403 (SMOW), respectively.

404 *4.2.2 In situ S isotope analysis*

405 In situ S isotope analysis was undertaken at the Key Laboratory of Earth and
406 Planetary Physics, Institute of Geology and Geophysics, CAS, using a
407 CAMECA NanoSIMS. The measurements were made using 3 different settings
408 of the Faraday cups/electron multiplier (EM) detectors, in order to meet the
409 diverse requirements for spatial resolution. The standard-sample-standard
410 bracketing method was applied to correct for instrumental mass fractionation.
411 Target spots of the most homogeneous isotopes (such as ^{32}S, ^{34}S and ^{75}As in
412 Fig. 9) were selected for in situ S isotope analysis in order to obtain the most
413 credible data. Internal standards included PY-1117 (pyrite), CS01 (pyrite), JC-

14 (sphalerite) and MY09-12 (sphalerite), and international standards included Balmat (pyrite and sphalerite) and CAR 123 (pyrite). The analytical precision calculated from replicate analyses of the unknown samples was better than 0.2‰ (1σ). The in situ S isotopic compositions were reported relative to the Vienna Canyon Diablo Troilite (V-CDT) standard. Details of instrument parameters and NanoSIMS in situ S isotope analysis techniques were described in Zhang et al. (2014).

4.2.3 Bulk S isotope analysis

Bulk S isotope analysis was undertaken at the SKLODG, IGCAS, using a Finnigan MAT-253 mass spectrometer. Sulfide mineral powders (200 mesh) were mixed with CuO powder, and then were heated to extract SO_2. The analytical uncertainty was better than 0.1‰ (1σ) calculated from replicate analyses of the IAEA international standards: IAEA S1 (-0.3‰), IAEA S2 (+22.62‰) and IAEA S3 (-32.49‰). The analytical precision calculated from replicate analyses of the unknown samples is better than 0.2‰ (2σ). The bulk $\delta^{34}S$ values are reported relative to the Vienna Canyon Diablo Troilite (V-CDT) standard.

4.2.4 In situ Pb isotope analysis

In situ Pb isotopes were analyzed at the State Key Laboratory of Continental Dynamics, Northwest University, using a Nu II MC-ICPMS instrument combined with a 266 nm femtosecond (fs) laser ablation system. The surface of the polished thin sections was cleaned with milli-Q water (18.2 MΩ·cm). Line scan

ablation consisted of background collection for 20 s followed by 50 s of laser ablation for signal collection. Laser ablation parameters were: 15 μm spot size for galena; 100% output energy, >600 μJ; 100% energy density, 6 J/cm^2; laser frequency, 5-50 Hz; and ablation way, line 3 μm/s. These ensured a strong enough Pb signal for the in situ analysis of galena samples. The Tl (20 ppb), NIST SRM 997 (^{205}Tl/^{203}Tl = 2.38890) and NIST SRM 610 glass served as internal and external standards. The repeated analyses of NIST SRM 610 glass yielded highly reliable and reproducible results during the whole analytical process with mean ^{206}Pb/^{204}Pb = 17.052 ± 0.003, ^{207}Pb/^{204}Pb = 15.515 ± 0.003 and ^{208}Pb/^{204}Pb = 36.980 ± 0.007 (1 s, *n* = 183). Details of instrument parameters and fs LA-MC-ICP-MS in situ Pb isotope analyses were described in Bao et al. (2016).

5. Analytical results

5.1 Bulk C-O isotopic compositions

Bulk δ^{13}C and δ^{18}O values of syn-ore calcite separates and fresh limestone whole-rock samples are listed in Table 1 and are shown in Figure 10. Syn-ore calcite (generation II) separates have δ^{13}C and δ^{18}O values ranging from +2.57 to +3.01‰ and +16.83 to +19.92‰, respectively. δ^{13}C and δ^{18}O values of fresh limestone whole-rock samples range from +1.58 to +2.63‰ and +21.85 to +24.01‰, respectively. The δ^{13}C values of syn-ore calcite can be compared with those of fresh limestone, but the former has slightly lower δ^{18}O values than

458 those of the latter (Fig. 10).

459 ***5.2 In situ and bulk $\delta^{34}S$ values***

460 In situ and bulk $\delta^{34}S$ values are presented in Table 2 and are shown in Figures
461 11-12. The NanoSIMS in situ $\delta^{34}S$ values of sulfide minerals range from +9.8 to
462 +23.1‰, of which pyrite and sphalerite crystals have $\delta^{34}S$ values ranging from
463 +10.3 to +19.4‰ and +9.8 to +23.1‰, respectively. In situ $\delta^{34}S$ values of pyrite-
464 I and pyrite-II crystals range from +12.8 to +19.4‰ and +10.3 to +10.4‰,
465 respectively. Sphalerite-I and sphalerite-II crystals have in situ $\delta^{34}S$ values
466 ranging from +12.5 to +23.1‰ and +9.8 to +16.9‰, respectively. A principal
467 feature of both pyrite and sphalerite crystals is that their $\delta^{34}S$ values decrease
468 gradually from core to rim (pyrite: decreasing from +19.4 to +10.3‰; sphalerite:
469 decreasing from +23.1 to +9.8‰; Figs. 11 and 12a). Sulfide minerals have bulk
470 $\delta^{34}S$ values ranging from +10.04 to +16.43‰, of which sphalerite has $\delta^{34}S$
471 values (+14.16-+16.43‰) higher than those of galena (generation II: +10.04-
472 +11.86‰). Sphalerite-I has bulk $\delta^{34}S$ values (+14.16-+16.43‰) similar to those
473 of sphalerite-II (+14.21-+15.10‰). Another major feature is that bulk S isotopic
474 data of sphalerite have a much narrower range than in situ S isotopic data (Fig.
475 11a-b).

476 ***5.3 In situ Pb isotopic compositions***

477 In situ Pb isotopic ratios of galena are listed in Table 3 and are shown in Figures
478 13-14. Galena (generation I and II) crystals have in situ $^{206}Pb/^{204}Pb$ ratios of
479 18.572-18.617, $^{207}Pb/^{204}Pb$ ratios of 15.711-15.728 and $^{208}Pb/^{204}Pb$ ratios of

38.592-38.727. In situ Pb isotopic ratios of galena-I are as follows: $^{206}Pb/^{204}Pb$ = 18.572-18.598, $^{207}Pb/^{204}Pb$ = 15.711-15.728 and $^{208}Pb/^{204}Pb$ = 38.592-38.695 and in situ Pb isotopic ratios of galena-II are: $^{206}Pb/^{204}Pb$ = 18.580-18.617, $^{207}Pb/^{204}Pb$ = 15.712-15.727, and $^{208}Pb/^{204}Pb$ = 38.597-38.727. The main feature is that $^{206}Pb/^{204}Pb$ and $^{208}Pb/^{204}Pb$ ratios of galena-I are lower than those of galena-II (Fig. 14a-b).

6. Discussion

6.1 Sources of ore-forming elements and associated fluids

6.1.1 New insights from C-O isotopes

Mineralogical records reveal that calcite and dolomite are the two main C-bearing minerals in the sulfide ores (Figs. 4-8). Thus, HCO_3^- and H_2CO_3 [occurring as CO_2 (aqueous)] are two dominant C species in the hydrothermal fluid, as supported by the analysis of fluid inclusions in sphalerite (Li ZL unpublished data). Therefore, the calculated $\delta^{13}C_{CO2}$ value is approximate to the theoretical $\delta^{13}C_{fluid}$ value, namely $\delta^{13}C_{CO2} \approx \delta^{13}C_{fluid}$, if the fractionation of C isotopes between HCO_3^- (liquid) or H_2CO_3 and CO_2 (gas) is negligible (Ohmoto, 1972; Hoefs, 2009). The $\delta^{13}C_{CO2}$ values were calculated using the temperature function of $1000 \ln\alpha_{(CO2\text{-}Calcite)} = -2.4612 + 7.663 \times 10^3 / (t + 273.15) - 2.988 \times 10^6 / (t + 273.15)^2$ (Bottinga, 1968; “t” [200 °C] is an average homogenization temperature of fluid inclusions in sphalerite, Li ZL unpublished data). Similarly, the $\delta^{18}O_{H2O}$ values were calculated using the temperature function of 1000 lnα

$_{(Calcite\text{-}H2O)}$ = 2.78 × 10^6 / (t + 273.15)^2 - 3.39 (O'Neil et al., 1969). We obtained $\delta^{13}C_{fluid}$ and $\delta^{18}O_{fluid}$ values having a range of +2.96-+3.40‰ and +7.80-+10.89‰, respectively (Table 2; Fig. 10).

It has been well-documented that $\delta^{13}C$ and $\delta^{18}O$ values of different geological reservoirs are distinct (Fig. 10). For instance, typical marine carbonate rocks have $\delta^{13}C$ values of -4-+4‰ and $\delta^{18}O$ values of +20-+30‰ (Veizer and Hoefs, 1976), the $\delta^{13}C$ and $\delta^{18}O$ values of mantle-derived CO_2 range from -8 to -4‰ and +6 to +10‰, respectively (Taylor et al., 1967; Demény et al., 1998), whereas sedimentary organic matters have $\delta^{13}C$ and $\delta^{18}O$ values mainly ranging from -30 to -15‰ and +24 to +30‰, respectively (Kump and Arthur, 1999; Hoefs, 2009). Therefore, C-O isotopes can provide an important constraint on the source of ore-forming fluids.

Compared with the above three main reservoirs of CO_2, the calculated $\delta^{13}C_{fluid}$ values (+2.96-+3.40‰) are higher than those of organic matters and the mantle, but are similar to those of carbonate rocks and limestone (Fig. 10). However, the calculated $\delta^{18}O_{fluid}$ values (+7.80-+10.89‰) are lower than those of organic matters, carbonate rocks and limestone (Fig. 10), but are similar to those of mantle or metamorphic fluids (+2-+25‰: Hoefs, 2009). This means that C is mainly derived from limestone, whereas the O isotope signature may be related to water/rock (W/R) interaction between mantle and/or metamorphic fluids and limestone.

Geologically, the mantle-derived basalts of the ELIP and the metamorphic rocks

524 of the Mesoproterozoic Kunyang Group are spatially associated with Pb-Zn
525 deposits in the Fule region (Figs. 1b, 2-3), suggesting that both mantle
526 magmatism and metamorphism have the potential to provide elements and
527 associated fluids to the hydrothermal system, as suggested in other places
528 (Pirajno, 2000; Davidheiser-Kroll et al., 2014). In addition, the occurrence of
529 abundant Cu and Ni sulfide minerals (Figs. 6-8) indicates a genetic relationship
530 between Emeishan magmatism and Pb-Zn mineralization. Furthermore,
531 evidence from in situ Pb isotopic data suggests that the metal Pb was derived
532 from a well-mixed source involving the basalts, sedimentary rocks and
533 metamorphic rocks (see below). Therefore, we propose that the O isotope
534 signature was generated by W/R interaction between mixed (mantle and
535 metamorphic) fluids and limestone.

536 *6.1.2 Constraints from in situ and bulk S isotopes*

537 Primary ore in the Fule deposit is composed of sphalerite, galena, pyrite, and
538 Cu and Ni sulfide minerals, but lacks sulfate minerals (Figs. 4-8). Hence, the
539 $\delta^{34}S$ values of sulfide minerals approximate those of the corresponding fluids,
540 namely $\delta^{34}S_{sulfide} \approx \delta^{34}S_{fluid}$ (Ohmoto, 1972; Seal, 2006). The $\delta^{34}S$ values of
541 sulfide minerals obtained by NanoSIMS in situ analyses compared with bulk
542 techniques range from +9.8 to +23.1‰ (average +15.5‰) and +10.04 to +16.43‰
543 (average +13.3‰), respectively (Figs. 11-12), reflecting the enrichment of
544 heavy S isotopes in the hydrothermal fluids. The mean $\delta^{34}S$ value of sulfide
545 minerals is +14.8‰, which approximates that of the ore-forming fluids. Such S

546 isotope signatures differ from mantle-derived S (0 ± 3‰: Chaussidon et al.,
547 1989), and are similar to Permian seawater (+11-+15‰: Claypool et al., 1980;
548 Seal, 2006). Given that the S was completely sourced from Permian seawater,
549 as the thermochemical sulfide reduction (see below) can form up to +15‰ of
550 the $\Delta^{34}S_{sulfate\text{-}sulfide}$ value (Ohmoto et al., 1990; Machel et al., 1995; Worden et
551 al., 1995; Ohmoto and Goldhaber, 1997), so the theoretical $\delta^{34}S_{sulfide}$ value
552 could drop to -4‰. The theoretically predicted $\delta^{34}S_{sulfide}$ values (-7-+15‰) do
553 not match well with the observed $\delta^{34}S$ values (+9.8-+23.1‰). Hence, Permian
554 seawater was not the only S source for the Fule deposit.
555 Previous studies suggested that the sulfate-bearing evaporites (salt-gypsum
556 rocks) that are common in the late Ediacaran to Triassic marine strata in the
557 region, with $\delta^{34}S$ values ranging from +22 to +28‰ (Fig. 11c; Zhou et al., 2013c),
558 overlap with those of the Ediacaran to Triassic seawater (+10-+35‰: Claypool
559 et al., 1980; Seal, 2006). If the S was totally derived from the above evaporites
560 or seawater, the theoretical $\delta^{34}S_{sulfide}$ values (+7-+28‰ or -5-+35‰) can match
561 reasonably well with the observed $\delta^{34}S$ values (+9.8-+23.1‰). Evidence from
562 S isotopes for the nearby Pb-Zn deposits (Fig. 12c), including the Shaojiwan
563 (hosted in early Permian) (Zhou et al., 2013c), Huize (hosted in early
564 Carboniferous) (Li et al., 2006, 2007), Nayongzhi (hosted in early Cambrian and
565 late Ediacaran) (Jin et al., 2016) and Maozu (hosted in late Ediacaran) (Zhou
566 et al., 2013b), also suggests that the S in the hydrothermal fluids was derived
567 from multiple S reservoirs. Hence, we conclude that the S in the Fule deposit

568 had multiple sources.

569 Thermochemical sulfate reduction (TSR) and bacterial sulfate reduction (BSR)
570 are two crucial processes for the formation of S^{2-} from SO_4^{2-}, and they are
571 temperature-dependent (Ohmoto et al., 1990; Machel et al., 1995; Hoefs, 2009;
572 Zhou et al., 2013c). TSR occurs at a relatively high temperature (higher than
573 100-140°C: Machel et al., 1995; Worden et al., 1995) and can generate a large
574 amount of S^{2-} with relatively stable $\delta^{34}S$ values (Ohmoto et al., 1990; Seal, 2006;
575 Zhou et al., 2013c). BSR occurs at a relatively low temperature (lower than
576 110°C: e.g. Jørgenson et al., 1992; Worden et al., 1995; Basuki et al., 2008).
577 As the metallogenic temperature (180-210°C, based on fluid inclusions in
578 sphalerite-II: Li ZL unpublished data) is too high for bacteria to survive, hence
579 BSR played an insignificant role in the formation of S^{2-}. In addition, the sulfide
580 ore reserves of the Fule deposit are more than 10 Mt, which suggests a
581 significant requirement of S^{2-}. This means that TSR has played a crucial role in
582 the formation of S^{2-} from SO_4^{2} in the Fule deposit.

583 The $\delta^{34}S$ values of pyrite-I crystals (rims: +12.8-+13.4‰) are higher than those
584 of paragenetic sphalerite-I crystals (rims: +12.5‰) in sample Fl_{14}-95 (Fig. 11).
585 Similarly, in sample Fl_{14}-65 (Fig. 11), pyrite-II crystals have $\delta^{34}S$ values (rims:
586 +10.3-+10.4‰) higher than those of paragenetic sphalerite-II crystals (rims:
587 +9.8-+10.1‰). Such S isotope signatures suggest that the fractionation of S
588 isotopes between pyrite and paragenetic sphalerite reached equilibrium
589 (Ohmoto, 1972; Seal, 2006). In addition, sphalerite-II has $\delta^{34}S$ values (+14.21-

590 +15.10‰) higher than those of galena-II (+10.04-+11.86‰) (Fig. 12a), which
591 indicates that S isotope fractionation between sphalerite and galena had also
592 reached equilibrium (Seal, 2006; Hoefs, 2009). Hence, equilibrium fractionation
593 played an important role in the variation of $\delta^{34}S$ values for the sulfide minerals
594 in the Fule deposit. On the other hand, the $\delta^{34}S$ values decrease gradually from
595 core to rim in both sphalerite and pyrite crystals (Fig. 11), which suggests that
596 other factors may have controlled the S isotope signatures, such as changes in
597 the physico-chemical conditions (T, pH, f_{O2}, f_S, etc.), Rayleigh fractionation, or
598 mixing of multiple S reservoirs (Ohmoto, 1972; Hoefs, 2009). Previous studies
599 suggested that physical and chemical conditions are crucial factors that can
600 cause large variations in S isotopes (Seal, 2006; Hoefs, 2009). However, the
601 circulating process (dissolution and re-precipitation) of local carbonate rocks
602 that was caused by water/rock (W/R) interaction (O'Neil et al., 1969; Zheng and
603 Hoefs, 1993; Warren, 2000) can help keep a metastable metallogenic
604 environment (see below). Hence, changes in physical-chemical conditions can
605 be ruled out. In contrast, as a consequence of dynamic fractionation, heavy S
606 isotopes are expected to be more enriched in the cores of sulfide minerals than
607 their rims (Figs. 11-12) during precipitation, due to the fact that light S isotopes
608 are more enriched in the gas phase (H_2S) (Seal, 2006; Zhou et al., 2013c).
609 Alternatively, a mixing process of multiple reservoirs and associated fluids can
610 cause distinct variation of S isotopes (Basuki et al., 2008; Zhou et al., 2013c),
611 and our isotopic data imply that multiple reservoirs were involved (Figs. 11-12),

providing the S source for the formation of the Fule sulfide ore. Therefore, both equilibrium and dynamic fractionation of S isotopes occurred during sulfide precipitation.

6.1.3 Evidence from in situ Pb isotopes

The extremely low U and Th contents in sulfide minerals (Carr et al., 1995; Muchez et al., 2005; Zhou et al., 2013a; Pass et al., 2014) enables us to use the Pb isotopic ratios of galena formed at different paragenetic stages in the Fule deposit to investigate the nature of the hydrothermal fluids. Uniform in situ Pb isotopic ratios of galena suggest a single or a well-mixed source of Pb (Fig. 13). The Pb isotopic data plot above the Pb evolution curve of the average upper continental crust in the diagram of $^{207}Pb/^{204}Pb$ vs. $^{206}Pb/^{204}Pb$ (Fig. 13) (Zartman and Doe, 1981).

Previous studies suggested that there are three potential metal sources in the SYG province, namely the late Permian Emeishan basalts, ore-hosting late Ediacaran to middle Permian sedimentary rocks and Meso- to Neo-proterozoic metamorphic rocks (Zheng and Wang, 1991; Zhou et al., 2001, 2013a; Huang et al., 2004; Li et al., 2007, 2015, 2016; Zhang et al., 2015; Jin et al., 2016; Zhu et al., 2017). Compared with the basalts, sedimentary rocks and basement rocks, galena has Pb isotopic ratios that differ from all of them in the diagram of $^{207}Pb/^{204}Pb$ vs. $^{206}Pb/^{204}Pb$ (Fig. 13). This means that there was not a single source for the Pb. In addition, galena displays higher $^{207}Pb/^{204}Pb$ than those of the basalts and basement rocks at a given $^{206}Pb/^{204}Pb$ ratio (Fig. 13), but both

634 the galena and the basalts, sedimentary rocks and basement rocks have the
635 same $^{206}Pb/^{204}Pb$ ratio at a given $^{206}Pb/^{204}Pb$ ratio (Fig. 13). It should be noted
636 that many of the ELIP basalts show evidence of crustal contamination and that
637 it is possible the contamination originated from carbonate rocks (possibly their
638 fluids) (Xu et al., 2001; Pirajno, 2013; Shellnutt, 2014). Hence, we cannot rule
639 out contribution from the ELIP basalts (6-323 μg/g Cu, 66-156 μg/g Zn and 3-
640 30 μg/g Pb: Huang et al., 2004; Xu et al., 2001, 2007) and we consider a well-
641 mixed metal source is a reasonable postulate (Fig. 13).
642 There is a gradual increase in the $^{206}Pb/^{204}Pb$ and $^{208}Pb/^{204}Pb$ ratios from
643 galena-I to galena-II (Fig. 14a-b), which can be explained by: (a) a high
644 $^{206}Pb/^{204}Pb$ and $^{208}Pb/^{204}Pb$-enriched source provided more Pb for galena-II
645 than galena-I, or (b) galena-I had lower ^{238}U and ^{232}Th contents than galena-II.
646 Because of the low U and Th contents in galena, and the lack of any distinct
647 difference between the two generations of galena (Zhou et al., 2011; Ye et al.,
648 2011 and unpublished data), so a highly radiogenic Pb-enriched source (such
649 as basalts or basements), which may have provided more Pb to the
650 hydrothermal fluids in the late phase is possible. This explanation is further
651 supported by the occurrence of abundant Cu and Ni sulfide minerals in the late
652 phase (Figs. 6-8).

653 ***6.2 Precipitation mechanisms of hydrothermal minerals***

654 *6.2.1 Mechanisms of calcite precipitation*

655 As the solubility of calcite decreases with increase in temperature, so cooling

656 of the fluid itself could not cause calcite precipitation (Zheng, 1990; Barnes,
657 1997; Hoefs, 2009). There are three main processes that can lead to calcite
658 precipitation in an open hydrothermal system, i.e. fluid mixing, water/rock (W/R)
659 interaction and CO_2 degassing (Zheng and Hoefs, 1993; Huang et al., 2010; Du
660 et al., 2017). Our C isotopic data suggest that C is sourced mainly from the
661 limestone (Fig. 10). This means that the process of fluid mixing played an
662 insignificant role in calcite precipitation. As a consequence of W/R interaction,
663 the circulating process between dissolution and re-precipitation in carbonate
664 rocks can cause calcite precipitation, at least locally (Warren, 2000). Moreover,
665 such circulating processes of precipitation → dissolution → re-precipitation can
666 generate metastable conditions that are beneficial to the continuous formation
667 of sulfide ore (Zhou et al., 2018). In addition, the C-O isotopic evolution curve
668 of W/R interaction between fluids (initial $\delta^{13}C_{fluid}$ = +2‰, $\delta^{18}O_{fluid}$ = +6‰) and
669 limestone (Fig. 15) was simulated, using the fractionation factor and equation
670 of C-O isotopes (O'Neil et al., 1969; Zheng and Hoefs 1993). The simulation
671 results suggest that our C-O isotopic data match well with the evolution curves
672 of both HCO_3^- and H_2CO_3 (Fig. 15) as the dominant C species (Zheng and
673 Hoefs, 1993). Similarly, the C-O isotopic evolution curve of CO_2 degassing (with
674 0.1, 0.2, 0.3 and 0.4 mol fraction of total C and O; initial $\delta^{13}C_{fluid}$ = +2‰, $\delta^{18}O_{fluid}$
675 = +6‰) was also simulated (Fig. 16a-b). The results show that our C-O isotopic
676 data still match well with the evolution curve of both H_2CO_3 (Fig. 16a) and HCO_3^-
677 (Fig. 16b) as the dominant C species. Hence, calcite precipitation was

controlled by both W/R interaction and CO_2 degassing.

6.2.2 Mechanisms of sulfide precipitation

Previous studies suggested that there are three main models (reduced S, local sulfate reduction, and mixing of metal and reduced S) that can account for sulfide precipitation in hydrothermal systems (Anderson, 1975; Corbella et al., 2004; Leach et al., 2005). The reduced S model requires metal and reduced S to be transported together to the depositional site; the local sulfate reduction model calls upon increasing the concentration of reduced S at the depositional site through sulfate reduction; and the mixing of metal and reduced S demands a metal-rich, but reduced S-poor brine, mixed with a fluid rich in hydrogen sulfide at the depositional site (Heijlen et al., 2003; Leach et al., 2005). Our S isotopic data suggest that S was derived from multiple reservoirs and TSR played a dominant role in the formation of S^{2-} from SO_4^{2-} (Figs. 11-12). However, our Pb isotopic data indicate that a well-mixed source of the basalts, sedimentary rocks and basement rocks provided the main metal source (Figs. 13-14). As the normal SO_4^{2-}-bearing basin brines are of low temperature (usually < 100 °C) (Corbella et al., 2004; Leach et al., 2005), which is lower than the required temperature for activating TSR, so the aforementioned three models cannot reasonably explain the formation of sulfide ore in the Fule deposit. Therefore, an alternative model is proposed here, namely fluid mixing caused by TSR, which then resulted in sulfide precipitation.

6.3 Possible mineralizing age and related geological events

In the Fule mining area, the ore-bearing strata are the middle Permian Yangxin Formation (Figs. 2-3), which implies that the ore formation time was not older than middle Permian age. In addition, the evidence from mineralogy (Cu and Ni sulfide minerals) (Figs. 6g, i, k, m, r-t and 7g-h, j, l-s), and O (Fig. 10) and Pb isotopes (Figs. 13-14) reveals a genetic association with Emeishan magmatism. This reflects that mineralization may have occurred at the same time as the ELIP. The most reliable radiometric dates indicate generation of the ELIP at 263-259 Ma (Xu et al., 2001; Zhou et al., 2002; Ali et al., 2005; Shellnutt et al., 2012). On the other hand, sulfide ore in the Fule deposit occurs as stratiform to lentiform shapes or as veins along the bedding-planes, locally associated with the Mile-Shizong-Shuicheng regional fault system and the Faben anticline (Figs. 1b, 2-3). These structures were activated during the Indosinian Orogeny (Lu et al., 2015), which suggests that the Fule deposit was most likely formed during the Indosinian period (257-200 Ma: Carter et al., 2001; Enkelmann et al., 2007; Reid et al., 2007; Lepvrier et al., 2008; Pullen et al., 2008). Furthermore, according to the Pb model ages, Si et al. (2006) considered that the Fule deposit was probably formed during late Triassic to early Jurassic (~225-198 Ma). This age broadly matches the dates of the nearby Pb-Zn deposits (245-192 Ma) (Guan and Li, 1999; Li et al., 2007; Lin et al., 2010; Mao et al., 2012; Zhou et al., 2013a, 2013b, 2015; Zhang et al., 2015), native Cu deposits (230-225 Ma) (Zhu et al., 2007) and Carlin-like Au deposits (235-204 Ma) (Chen et al., 2015). Hence, the Fule and nearby deposits were formed between 250-200

722 Ma, and were most likely related to the ELIP and the Indosinian Orogeny that
723 occurred after eruption of the Emeishan basalts.

724 ***6.4 Ore genesis***

725 Sulfide ore in the Fule deposit has a spatial association with the Emeishan
726 basalts (Figs. 1b, 2-3), which led some researchers to classify it as a distal
727 magmatic-hydrothermal type (Xie, 1963). Other geological evidence linking
728 mineralization to Emeishan magmatism includes the occurrence of hidden Pb-
729 Zn veins in the basalts at Xuanwei County, NE Yunnan Province (Liu and Lin,
730 1999). On the other hand, sulfide ore in the Fule deposit occurs in stratiform to
731 lentiform shapes or veins (Figs. 3-4) that are clearly stratabound. This led other
732 researchers to classify it as a Sedimentary Exhalative-type (SEDEX) or a
733 stratabound-type of deposit (Si et al., 2006). However, the Fule sulfide ore is
734 hosted by middle Permian carbonate rocks, which are different from clastic
735 rocks that host sulfide ore of SEDEX-type (Leach et al., 2005). In addition,
736 based on the evidence of Cd isotopes, the Fule deposit was considered to be
737 a Mississippi Valley-type (MVT) deposit (Zhu et al., 2017). Traditionally, typical
738 MVT deposits are related to basin fluids that are characterized by low
739 temperatures (50-200 °C) and high salinities (10-30 wt. % NaCl equiv.) and
740 have no genetic association with magmatic activity (Leach et al., 2005, 2010).
741 However, the study of fluid inclusions in sphalerite suggests that the ore-forming
742 fluids in the Fule deposit are characterized by low-medium temperatures (120-
743 260 °C) and low salinities (4-10 wt. % NaCl equiv.) (Si et al., 2006; Li ZL,

744 unpublished data). In addition, the occurrence of abundant Cu and Ni sulfide
745 minerals (Figs. 6g, i, k, m, r-t and 7g-h, j, l-s), and the evidence of O (Fig. 10)
746 and Pb isotopes (Figs. 13-14) imply that the formation of sulfide ore in the Fule
747 deposit was associated with the ELIP. Furthermore, these features are similar
748 to those of the unique SYG-type Huize Pb-Zn deposit (Zhou et al., 2001; Huang
749 et al., 2004; Li et al., 2007) (Table 4). Moreover, the sulfide ore in the Fule
750 deposit is of higher grades (up to 60 wt. % Zn + Pb, av. 15-20 wt. %) than those
751 of MVT deposits (usually < 10. Wt. % Zn + Pb). Hence, we propose that the
752 Fule deposit is not a typical MVT deposit and represents a new unique SYG-
753 type of deposit that is between MVT and magmatic hydrothermal deposits.

754 ***6.5 Ore formation process and relationship with the ELIP***

755 Pirajno (2000) established indirect links with sediment-hosted deposits (such
756 as MVT and SEDEX-type) and mantle plumes. The thermal simulation indicates
757 that the basalts of the EILP begin to release metal-bearing fluids at ~5-10 Ma
758 after it erupting and this process can last over ~50 Ma (Xu et al., 2014). On the
759 other hand, if we consider that the Pb-Zn deposits in the ELIP formed as a
760 consequence of Indosinian tectonism (~257-200 Ma: Carter et al., 2001;
761 Lepvrier et al., 2004; Enkelmann et al., 2007; Reid et al., 2007; Pullen et al.,
762 2008), then it makes sense that magmatic fluids related to the Emeishan event
763 could pass through the carbonate rocks and be involved in the mineralization.
764 Furthermore, metal-bearing fluids (including thermal flux and volatiles)
765 generated by Emeishan magmatism have been shown to be involved in the

766 formation of the Fule deposit, as evidenced by field data (Figs. 1-8), fluids
767 compositions (Figs. 10, 12, 15-16), and in situ S (Figs. 9, 11-12) and Pb (Figs.
768 13-14) isotopes. In addition, hydrothermal fluids responsible for carbonate-
769 hosted base metal deposits in the Irish Pb-Zn ore district was considered to be
770 driven by mantle heat (Davidheiser-Kroll et al., 2014). Hence, sulfide ore in the
771 Fule deposit has a genetic relationship with Emeishan magmatism.
772 Between 263-259 Ma, during the eruption of the Emeishan basalts (Shellnutt,
773 2014), fluids were provided (thermal flux + volatiles) and there was an elevated
774 background geothermal gradient, both of which facilitated and enhanced the
775 mobilization and extraction of ore-forming elements from Proterozoic
776 metamorphic rocks in the basement and Paleozoic sedimentary rocks (Fig.
777 17a). Following eruption of the Emeishan basalts, these metal-bearing mixed
778 (mantle and metamorphic) fluids (initial $\delta^{13}C_{fluid}$ = +2‰, $\delta^{18}O_{fluid}$ = +6‰) were
779 driven upward along regional faults (including the Mile-Shizong-Shuicheng fault
780 and its subsidiaries; Fig. 1a) during the early Indosinian Orogeny (257-250 Ma)
781 (Fig. 17b). These fluids were then released into structural units (such as the
782 Faben anticline) when the overall tectonic regime changed from compression
783 to extension between 250-200 Ma (Fig. 17c) (Carter et al., 2001; Reid et al.,
784 2007; Lepvrier et al., 2008; Lu et al., 2015; Qiu et al., 2016). The fluids were
785 then trapped by evaporitic salt and sedimentary organic-bearing units within the
786 platform carbonate sequences at the structurally-controlled depositional sites
787 (Fig. 17c). This process resulted in the formation of S^{2-} from multiple S

reservoirs via TSR and the extraction of some metals from ore-hosting strata through W/R interaction (as evidenced by C-O-S and Pb isotopes), and then resulted in the precipitation of hydrothermal minerals (Fig. 17c). Importantly during ore formation, the Emeishan basalts also acted as an impermeable and protective layer (Figs. 1b, 2-3, 17) and even acted as ore-hosting rocks, which enabled the massive accumulation of Cu, Pb-Zn, and even Au ores in the western Yangtze Block (Fig. 1b).

7. Conclusions

(a) Bulk C-O isotopic data suggest that the source of C in the Fule Pb-Zn deposit was limestone, whereas the O isotope signature is related to W/R interaction between mixed (mantle and metamorphic) fluids and limestone. W/R interaction and CO_2 degassing are two crucial processes for calcite precipitation.

(b) Both in situ and bulk S isotopic data indicate a mixed S source from multiple reservoirs and that TSR played a crucial role in the formation of S^{2-}. Both equilibrium and dynamic fractionation controlled the variation in S isotopes.

(c) In situ Pb isotopic data imply a well-mixed Pb source that includes basalts, sedimentary rocks and Proterozoic basement rocks.

(d) The Fule Pb-Zn deposit thus represents a new unique SYG-type of deposit that is between MVT and magmatic hydrothermal deposits.

Acknowledgements:

This research was financially supported by the National Key Research and Development Project of China (2017YFC0602502), the Key Program of National Natural Science Foundation of China (41430315), the National Basic Research Program of China (2014CB440905), and the Visiting Scholar Project of China Scholarship Council to Jia-Xi Zhou (201604910455). We thank Profs. Lin Ye (IG CAS) and Mei-Fu Zhou (University of Hong Kong) for fruitful discussions. We thank Prof. Franco Pirajno (Associate Editor), Prof. Greg Shellnutt and anonymous reviewers for their constructive suggestions and comments.

References

Ali, J.R., Thompson, G.M., Zhou, M.F., Song, X.Y., 2005. Emeishan large igneous province, SW China. Lithos 79, 475–489.

Anderson, G.M., 1975. Precipitation of Mississippi Valley-type ores. Economic Geology 70, 937–942.

Anderson, G.M., Macqueen, R.W., 1982. Ore deposit models-6. Mississippi Valley-type lead-zinc deposits. Geoscience Canada 9, 108–117.

Bai, J., Huang, Z., Zhu, D., Yan, Z., Zhou, J., 2013. Isotopic compositions of sulfur in the Jinshachang lead-zinc deposit, Yunnan, China, and its implication on the formation of sulfur-bearing minerals. Acta Geologica Sinica (English Edition) 87, 1355–1369.

832 Bao, Z., Li, Q., Wang, C.Y., 2017. Metal source of giant Huize Zn-Pb deposit in
833 SW China: New constraints from in situ Pb isotopic compositions of galena.
834 Ore Geology Reviews, https://doi.org/10.1016/j.oregeorev.2017.08.019.
835 Bao, Z., Yuan, W., Yuan, H., Liu, X., Chen, K., Zong, C., 2016. Non-matrix-
836 matched determination of lead isotope ratios in ancient bronze artifacts by
837 femtosecond laser ablation multi-collector inductively coupled plasma
838 mass spectrometry. International Journal of Mass Spectrometry 402, 12–
839 19.
840 Barker, S.L., Hickey, K.A., Cline, J.S., Dipple, G.M., Kilburn, M.R., Vaughan,
841 J.R., Longo, A.A., 2009. Uncloaking invisible gold: Use of nanoSIMS to
842 evaluate gold, trace elements, and sulfur isotopes in pyrite from Carlin-type
843 gold deposits. Economic Geology 104, 897–904.
844 Barnes, H.L., 1997. Geochemistry of hydrothermal ore deposits. John Wiley &
845 Sons, v. 1.
846 Basuki, N.I., Taylor, B.E., Spooner, E.T.C., 2008. Sulfur isotope evidence for
847 thermo-chemical reduction of dissolved sulfate in Mississippi valley type
848 zinc-lead mineralization, Bongara area, northern Peru. Economic Geology
849 103, 183–799.
850 Bottinga, Y., 1968. Calculation of fractionation factors for carbon and oxygen
851 isotopic exchange in the system calcite-carbon dioxide-water. The Journal
852 of Physical Chemistry 72, 800–808.
853 Carr, G.R., Dean, J.A., Suppel, D.W., Heithersay, P.S., 1995. Precise lead

isotope fingerprinting of hydrothermal activity associated with Ordovician to Carboniferous metallogenic events in the Lachlan fold belt of New South Wales. Economic Geology 90, 1467–1505.

Carter, A., Roques, D., Bristow, C., Kinny, P., 2001. Understanding Mesozoic accretion in Southeast Asia: Significance of Triassic thermotectonism (Indosinian Orogeny) in Vietnam. Geology 29, 211–214.

Chaussidon, M., Albarède, F., Sheppard, S.M.F., 1989. Sulphur isotope variations in the mantle from ion microprobe analyses of micro-sulphide inclusions. Earth and Planetary Science Letters 92, 144–156.

Chen, K.Y., Yuan, H.L., Bao, Z.A., Zong, C.L., Dai, M.N., 2014. Precise and accurate *in situ* determination of lead isotope ratios in NIST, USGS, MPI-DING and CGSG glass reference materials using femtosecond laser ablation MC-ICP-MS. Geostandards and Geoanalytical Research 38, 5–21.

Chen, M., Mao, J., Li, C., Zhang, Z., Dang, Y., 2015. Re-Os isochron ages for arsenopyrite from Carlin-like gold deposits in the Yunnan-Guizhou-Guangxi “golden triangle”, southwestern China. Ore Geology Reviews 64, 316–327.

Claypool, G.E., Holser, W.T., Kaplan, I.R., Sakai, H., Zak, I., 1980. The age curves of sulfur and oxygen isotopes in marine sulfate and their mutual interpretation. Chemical Geology 28, 199–260.

Corbella, M., Ayora, C., Cardellach, E., 2004. Hydrothermal mixing, carbonate

876 dissolution and sulfide precipitation in Mississippi Valley-type deposits.
877 Mineralium Deposita 39, 344–357.
878 Davidheiser-Kroll, B., Stuart, F.M., Boyce, A.J., 2014. Mantle heat drives
879 hydrothermal fluids responsible for carbonate-hosted base metal deposits:
880 evidence from $^{3}He/^{4}He$ of ore fluids in the Irish Pb-Zn ore district.
881 Mineralium Deposita 49, 547–553.
882 Demény, A., Ahijado, A., Casillas, R., Vennemann, T.W., 1998. Crustal
883 contamination and fluid/rock interaction in the carbonatites of
884 Fuerteventura (Canary Islands, Spain): A C, O, H isotope study. Lithos 44,
885 101–115.
886 Deng, J., Wang, C., Bagas, L., Selvaraja, V., Jeon, H., Wu, B., Yang, L., 2017.
887 Insights into ore genesis of the Jinding Zn–Pb deposit, Yunnan Province,
888 China: Evidence from Zn and in-situ S isotopes. Ore Geology Reviews,
889 http://dx.doi.org/10.1016/j.oregeorev.2016.10.036.
890 Du, L.J., Li, B., Huang, Z.L., Zhou, J.X., Zou, G.F., Yan, Z.F., 2017. Carbon-
891 oxygen isotopic geochemistry of the Yangla Cu skarn deposit, SW China:
892 Implications for the source and evolution of hydrothermal fluids. Ore
893 Geology Reviews 88, 809–821.
894 Enkelmann, E., Weislogel, A., Ratschbacher, L., Eide, E., Renno, A., Wooden,
895 J., 2007. How was the Triassic Songpan-Ganzi basin filled? A provenance
896 study. Tectonic 26, doi:10.1029/2006TC002078.
897 Gao, S., Yang, J., Zhou, L., Li, M., Hu, Z.C., Guo, J.L., Yuan, H.L., Gong, H.J.,

898 Xiao, G.Q., Wei, J.Q., 2011. Age and growth of the Archean Kongling
899 terrain, South China, with emphasis on 3.3 Ga granitoid gneisses.
900 American Journal of Sciences 311, 153–182.
901 Guan, S.P., Li, Z.X., 1999. Pb and S isotope study of carbonate-hosted Pb-Zn
902 deposits at the eastern margin of the Kangdian axis. Geology
903 Geochemistry 27, 45–54 (in Chinese with English abstract).
904 Heijlen, W., Muchez, P., Banks, D.A., Schneider, J., Kucha, H., Keppens, E.,
905 2003. Carbonate-hosted Zn-Pb deposits in Upper SiJesia, Poland: Origin
906 and evolution of mineralizing fluids and constraints on genetic models.
907 Economic Geology 98, 911–932.
908 Hoefs, J., 2009. Stable isotope geochemistry (sixth edition). Springer-Verlag
909 Berlin Heidelberg, doi: 10.1007/978-3-540-70708-0.
910 Hu, R.Z., Zhou, M.F., 2012. Multiple Mesozoic mineralization events in South
911 China-an introduction to the thematic issue. Mineralium Deposita 47, 579–
912 588.
913 Hu, R., Fu, S., Huang, Y., Zhou, M., Fu, S., Zhao, C., Wang, Y., Bi, X., Xiao, J.,
914 2017. The giant South China Mesozoic low-temperature metallogenic
915 domain: Reviews and a new geodynamic model. Journal of Asian Earth
916 Sciences 137, 9–34.
917 Huang, Z.L., Chen, J., Han, R.S., Li, W.B., Liu, C.Q., Zhang, Z.L., Ma, D.Y., Gao,
918 D.R., Yang H.L., 2004. Geochemistry and ore genesis of the Huize giant
919 Pb-Zn deposit in Yunnan Province, China: Discussion on the relationship

between the Emeishan flood basalts and Pb-Zn mineralization. Geological Publishing House Beijing, pp. 1–214 (in Chinese).

Huang, Z., Li, X., Zhou, M., Li, W., Jin, Z., 2010. REE and C-O isotopic geochemistry of calcites from the word-class Huize Pb-Zn deposits, Yunnan, China: Implication for the ore genesis. Acta Geologica Sinica (English edition) 84, 597–613.

Ikehata, K., Notsu, K., Hirata, T., 2008. In situ determination of Cu isotope ratios in copper-rich materials by NIR femtosecond LA-MC-ICP-MS. Journal of Analytical Atomic Spectrometry 23, 1003–1008.

Jian, P., Li, D.Y., Kröner, A., Zhang, Q., Wang, Y.Z., Sun, X.M., Zhang, W., 2009. Devonian to Permian plate tectonic cycle of the Paleo-Tethys Orogen in southwest China (II): Insights from zircon ages of ophiolites, arc/back-arc assemblages and within-plate igneous rocks and generation of the Emeishan CFB province. Lithos 113, 767–784.

Jin, Z.G., 2008. The ore-control factors, ore-forming regularity and ore forecasting of Pb-Zn deposits in NW Guizhou province. Engine Industry Press, Beijing, pp. 1–105 (in Chinese).

Jin, Z.G., Zhou, J.X., Huang, Z.L., Ye, L., Luo, K., Gao, J.G., Chen, X.L., Wang, B., Peng, S., 2016. Ore genesis of the Nayongzhi Pb-Zn deposit, Puding city, Guizhou Province, China: Evidences from S and in situ Pb isotopes. Acta Petrologica Sinica 32, 3441–3455 (in Chinese with English abstract).

Jørgenson, B.B., Isaksen, M. F., Jannasch, H. W., 1992. Bacterial sulfate

reduction above 100°C in deep sea hydrothermal vent sediments. Science 258, 1756–1757.

Kump, L.R., Arthur, M.A., 1999. Interpreting carbon-isotope excursions: Carbonates and organic matter. Chemical Geology 161, 181–198.

Leach, D.L., Bradley, D.C., Huston, D., Pisarevsky, S.A., Taylor, R.D., Gardoll, S.J., 2010. Sediment-hosted lead-zinc deposits in Earth history. Economic Geology 105, 593–625.

Leach, D.L., Sangster, D., Kelley, K.D., Large, R.R., Garven, G., Allen, C., Gutzmer, J., Walters, S., 2005. Sediment-hosted lead-zinc deposits: A global perspective. Economic Geology 100th Anniversary, 561–607.

Lepvrier, C., Maluski, H., Tich, V.V., Leyreloup, A., Thi, P.T., Vuong, N.V., 2004. The early Triassic Indosinian orogeny in Vietnam (Truong Son Belt and Kontum Massif): Implications for the geodynamic evolution of Indochina. Tectonophysics 393, 87–118.

Lepvrier, C., Vuong, N.V., Maluski, H., Thi, P.T., Tich, V.V., 2008. Indosinian tectonics in Vietnam. Comptes Rendus Geoscience 340, 94–111.

Li, B., Zhou, J., Li, Y., Chen, A., Wang, R., 2016. Geology and Isotope Geochemistry of the Yinchanggou-Qiluogou Pb-Zn Deposit, Sichuan Province, Southwest China. Acta Geologica Sinica (English Edition) 90, 1768–1779.

Li, B., Zhou, J.X., Huang, Z.L., Yan, Z.F., Bao, G.P., Sun, H.R., 2015. Geological, rare earth elemental and isotopic constraints on the origin of the

964 Banbanqiao Zn-Pb deposit, southwest China. Journal of Asian Earth
965 Sciences 111, 100–112.
966 Li, W.B., Huang, Z.L., Yin, M.D., 2007. Dating of the giant Huize Zn-Pb ore field
967 of Yunnan province, southwest China: Constraints from the Sm-Nd system
968 in hydrothermal calcite. Resource Geology 57, 90–97.
969 Li, X.B., Huang, Z.L., Li, W.B., Zhang, Z.L., Yan, Z.F., 2006. Sulfur isotopic
970 compositions of the Huize super-large Pb-Zn deposit, Yunnan Province,
971 China: Implications for the source of sulfur in the ore-forming fluids. Journal
972 of Geochemical Exploration 89, 227–230.
973 Lin, Z.Y., Wang, D.H., Zhang, C.Q., 2010. Rb-Sr isotopic age of sphalerite from
974 the Paoma lead-zinc deposit in Sichuan Province and its implications.
975 Geology of China 37, 488–196 (in Chinese with English abstract).
976 Liu, H.C., Lin, W.D., 1999. Study on the law of Pb-Zn-Ag ore deposit in
977 northeast Yunnan, China. Yunnan University Press, Kunming, pp. 1–468
978 (in Chinese).
979 Liu, W. H., Zhang, J., Wang, J., 2017. Sulfur isotope analysis of carbonate-
980 hosted Zn-Pb deposits in northwestern Guizhou Province, Southwest
981 China: Implications for the source of reduced sulfur. Journal of
982 Geochemical Exploration 181, 31–44.
983 Lu, Y.H., Han, R.S., Ren, T., Qiu, W.L., Rang, H., Gao, Y., 2015. Ore-controlling
984 characteristics of fault structures and their relations to mineralization at
985 Fulechang Zn-Pb mining district in deposit concentration district of

northeastern Yunnan, China. Geoscience 29, 563–575.

Machel, H.G., Krouse, H.R., Sassen, R., 1995. Products and distinguishing criteria of bacterial and thermo-chemical sulfate reduction. Applied Geochemistry 10, 373−389.

Mao, J.W., Zhou, Z.H., Feng, C.Y., Wang, Y.T., Zhang, C.Q., Peng, H.J., Miao, Y., 2012. A preliminary study of the Triassic large-scale mineralization in China and its geodynamic setting. Geology of China 39, 1437−1471 (in Chinese with English abstract).

Muchez, P., Heijlen, W., Banks, D., Blundell, D., Boni, M., Grandia, F., 2005. Extensional tectonics and the timing and formation of basin-hosted deposits in Europe. Ore Geology Reviews 27, 241−267.

Nishizawa, M., Maruyama, S., Urabe, T., Takahata, N., Sano, Y., 2010. Micro-scale (1.5 μm) sulphur isotope analysis of contemporary and early Archean pyrite. Rapid Communications in Mass Spectrometry 24, 1397–1404.

Ohmoto, H., 1972 Systematics of Sulfur and Carbon Isotopes in Hydrothermal Ore Deposits. Economic Geology 67, 551–579.

Ohmoto, H., Goldhaber, M.B., 1997. Sulfur and carbon isotopes, in Barnes HL (Editor), Geochemistry of hydrothermal ore deposits, 3rd edition. Wiley, New York, pp. 517–611.

Ohmoto, H., Kaiser, C.J., Geer, K.A., 1990. Systematic of sulfur isotopes in recent marine sediments and ancient sediment-hosted base metal deposits In H. K Herbert and S. E. Ho (Editors), Stable isotopes and Fluid

1008 Processes in Mineralisation. Geol Dep Univ Extens, University of Western
1009 Australia 23, 70–120.
1010 O'Neil, J.R., Clayton, R.N., Mayeda, T.K., 1969. Oxygen isotope fractionation in
1011 divalent metal carbonates. Journal of Chemical Physics 51, 5547–5558.
1012 Pass, H.E., Cookem, D.R., Davidson, G., Maas, R., Dipple, G., Rees, C.,
1013 Ferreira, L., Taylor, C., Deyell, C.L., 2014. Isotope geochemistry of the
1014 northeast zone, Mount Polley alkalic Cu-Au-Ag porphyry deposit, British
1015 Columbia: A case for carbonate assimilation. Economic Geology 109, 859–
1016 890.
1017 Pirajno, F., 2000. Ore deposits and mantle plumes. Springer, Science &
1018 Business Media, pp. 1–572. Doi: 10.1007/978-94-017-2502-6.
1019 Pirajno, F., 2013. Large igneous provinces (Xiong'er, Dashigou, 827 Ma Event,
1020 Tarim, Emeishan) and the Yanshanian tectono-thermal event of eastern
1021 China. The Geology and Tectonic Settings of China's Mineral Deposits,
1022 Springer, Netherlands, pp. 547–638.
1023 Pullen, A., Kapp, P., Gehrels, G.E., Vervoort, J.D., Lin, D., 2008. Triassic
1024 continental subduction in central Tibet and Mediterranean-style closer of
1025 the Paleo-Tethys Ocean. Geology 36, 351–354.
1026 Qiu, L., Tang, S.L., Wang, Q., Yang, W.X., Tang, X.L., Wang, J.B., 2016.
1027 Mesozoic geology of southwestern China: Indosinian foreland
1028 overthrusting and subsequent deformation. Journal of Asian Earth
1029 Sciences 122, 91–105.

1030 Reid, A., Wilson, C.J.L., Shun, L., Pearson, N., Belousova, E., 2007. Mesozoic
1031 plutons of the Yidun Arc, SW China: U-Pb geochronology and Hf isotopic
1032 signature. Ore Geology Reviews 31, 88–106.
1033 Seal, I.R., 2006. Sulfur isotope geochemistry of sulfide minerals. Review of
1034 Mineralogy and Geochemistry 61, 633–677.
1035 Shellnutt, J.G., Denyszyn, S.W., Mundil, R., 2012. Precise age determination of
1036 mafic and felsic intrusive rocks from the Permian Emeishan large igneous
1037 province (SW China). Gondwana Research 22, 118–126.
1038 Shellnutt, J.G., 2014. The Emeishan large igneous province: A synthesis.
1039 Geoscience Frontiers 5, 369–394.
1040 Si, R.J., Gu, X.X., Pang, X.C., Fu, S.H., Li, F.Y., Zhang, M., Li, Y.H., Li, X.Y., Li,
1041 J., 2006. Geochemical character of dispersed elements in sphalerite from
1042 Fule Pb-Zn polymetal deposit, Yunnan province. Journal of Mineralogy and
1043 Petrology 26, 75–80 (in Chinese with English abstract).
1044 Si, R.J., Gu, X.X., Xiao, C., Yu, H.T., Wang, Z.W., Chen, Y.J., Qiu, N., 2011.
1045 Geochemical character of trace elements in sphalerite from Fule Pb-Zn
1046 deposit, Yunnan province. Journal of Mineralogy and Petrology 31, 34–40
1047 (in Chinese with English abstract).
1048 Si, R.J., Gu, X.X., Xie, L.X., Zhang, N., 2013. Geological characteristics of the
1049 Fule polymetallic deposit in Yunnan province: A Pb-Zn deposit with
1050 dispersed elements and unusual enrichment. Geology and Exploration 49,
1051 313–322 (in Chinese with English abstract).

1052 Taylor, H.P., Frechen, J., Degens, E.T., 1967. Oxygen and carbon isotope
1053 studies of carbonatites from the Laacher See District, West Germany and
1054 the Alnö District, Sweden. Geochimica et Cosmochimica Acta 31, 407–430.
1055 Tang, Y.Y., Bi, X.W., Fayek, M., Hu, R.Z., Wu, L.Y., Zou, Z.C., Feng, C.X., Wang,
1056 X.S., 2014. Microscale sulfur isotopic compositions of sulfide minerals from
1057 the Jinding Zn-Pb deposit, Yunnan Province, Southwest China. Gondwana
1058 Research 26, 594–607.
1059 Tran, T.H., Polyakov, G.V., Tran, T.A., Borisenko, A.S., Izokh, A.E., Balykin, P.A.,
1060 Ngo, T.P., Pham, T.D., 2016. Intraplate magmatism and metallogeny of
1061 North Vietnam. Springer, Modern Approaches in Solid Earth Sciences,
1062 Dordrecht, pp. 1–381. Doi: 10.1007/978-3-319-25235-3.
1063 Veizer, J., Hoefs, J., 1976. The nature of O^{18}/O^{16} and C^{13}/C^{12} secular trends in
1064 sedimentary carbonate rocks. Geochimica et Cosmochimica Acta 40,
1065 1387–1395.
1066 Wang, C.M., Deng, J., Carranza, E.J.M., Lei, X.R., 2014. Nature, diversity and
1067 temporal-spatial distributions of sediment-hosted Pb-Zn deposit in China.
1068 Ore Geology Reviews 56, 327–351.
1069 Warren, J., 2000. Dolomite: occurrence, evolution and economically important
1070 associations. Earth Science-Review 52, 1–81.
1071 Wei, A.Y., Xue, C.D., Xiang, K., Li, J., Liao, C., Akhter, Q.J., 2015. The ore-
1072 forming process of the Maoping Pb-Zn deposit, northeastern Yunnan,
1073 China: Constraints from cathodoluminescence (CL) petrography of

hydrothermal dolomite. Ore Geology Reviews 70, 562–577.

Worden, R.H., Smalley, P.C., Oxtoby, N.H., 1995. Gas souring by the thermo chemical sulfate reduction at 140°C: AAPG Bulletin 79, 854–863.

Xie, J.R., 1963. Introduction of the Chinese Ore Deposits. Scientific Books Publishing House Beijing, pp. 1–71 (in Chinese).

Xu, Y., Chung, S.L., Jahn, B.M., Wu, G., 2001. Petrologic and geochemical constraints on the petrogenesis of Permian-Triassic Emeishan flood basalts in southwestern China. Lithos 58, 145–168.

Xu, J.F., Suzuki, K., Xu, Y.G., Mei, H.J., Li, J., 2007. Os, Pb, and Nd isotope geochemistry of the Permian Emeishan continental flood basalts: insights into the source of a large igneous province. Geochimica et Cosmochimica Acta 71, 2104–2119.

Xu, Y., Huang, Z., Zhu, D., Luo, T., 2014. Origin of hydrothermal deposits related to the Emeishan magmatism. Ore Geology Reviews 63, 1–8.

Yan, D.P., Zhou, M.F., Song, H.L., Wang, X.W., Malpas, J., 2003. Origin and tectonic significance of a Mesozoic multilayer overthrust system within the Yangtze Block (South China). Tectonophysics 361, 239–254.

Yan, Z.F., Huang, Z.L., Xu, C., Chen, M., Zhang, Z.L., 2007. Signatures of the source for the Emeishan flood basalts in the Ertan area: Pb isotope evidence. Chinese Journal of Geochemistry 26, 207–213.

Ye, L., Cook, N.J., Ciobanu, C.L., Liu, Y.P., Zhang, Q., Liu, T.G., Gao, W., Yang, Y.L., Danyushevsky, L., 2011. Trace and minor elements in sphalerite from

base metal deposits in South China: a LA–ICPMS study. Ore Geology Reviews 39, 188–217.

Yuan, H.L., Yin, C., Liu, X., Chen, K.Y., Bao, Z.A., Zong, C.L., Dai, M.N., Lai, S.C., Wang, R., Jiang, S.Y., 2015. High precision in-situ Pb isotopic analysis of sulfide minerals by femtosecond laser ablation multi-collector inductively coupled plasma mass spectrometry. Science in China, Earth Science 58, 1713–1721.

Zartman, R.E., Doe, B.R., 1981. Plumbotectonics-the model. Tectonophysics 75, 135–162.

Zaw, K., Peters, S.G., Cromie, P., Burrett, C., Hou, Z.Q., 2007. Nature, diversity of deposit types and metallogenic relations of South China. Ore Geology Reviews 31, 3–47.

Zhang, C., Wu, Y., Hou, L., Mao, J., 2015. Geodynamic setting of mineralization of Mississippi Valley-type deposits in world-class Sichuan-Yunnan-Guizhou Zn-Pb triangle, southwest China: Implications from age-dating studies in the past decade and the Sm-Nd age of the Jinshachang deposit. Journal of Asian Earth Sciences 103, 103–114.

Zhang, J., Lin, Y., Yang, W., Shen, W., Hao, J., Hu, S., Cao, M., 2014. Improved precision and spatial resolution of sulfur isotope analysis using NanoSIMS. Journal of Analytical Atomic Spectrometry 29, 1934–1943.

Zheng, Y.F., Hoefs, J., 1993. Carbon and oxygen isotopic covariations in hydrothermal calcites. Mineralium Deposita 28, 79–89.

1118 Zheng, Y.F., 1990. Carbon-oxygen isotopic covariation in hydrothermal calcite
1119 during degassing of CO_2. Mineralium Deposita 25, 246–250.
1120 Zheng, M.H., Wang, X.C., 1991. Genesis of the Daliangzi Pb-Zn deposit in
1121 Sichuan, China. Economic Geology 86, 831–846.
1122 Zhou, C.X., Wei, C.S., Guo, J.Y., 2001. The source of metals in the Qilingchang
1123 Pb-Zn deposit, Northeastern Yunnan, China: Pb-Sr isotope constraints.
1124 Economic Geology 96, 583–598.
1125 Zhou, J., Huang, Z., Zhou, G., Li, X., Ding, W., Bao, G., 2011. Trace elements
1126 and rare earth elements of sulfide minerals in the Tianqiao Pb-Zn ore
1127 deposit, Guizhou Province. China. Acta Geologica Sinica (English Edition)
1128 85, 189–199.
1129 Zhou, J., Huang, Z., Bao, G., Gao, J., 2013c. Sources and thermo-chemical
1130 sulfate reduction for reduced sulfur in the hydrothermal fluids, southeastern
1131 SYG Pb-Zn metallogenic province, SW China. Journal of Earth Science 24,
1132 759–771.
1133 Zhou, J.X., Huang, Z.L., Lv, Z.C., Zhu, X.K., Gao, J.G., Mirnejad, H., 2014b.
1134 Geology, isotope geochemistry and ore genesis of the Shanshulin
1135 carbonate-hosted Pb-Zn deposit, southwest China. Ore Geology Reviews
1136 63, 209–225.
1137 Zhou, J.X., Huang, Z.L., Yan, Z.F., 2013b. The origin of the Maozu carbonate-
1138 hosted Pb-Zn deposit, southwest China: Constrained by C-O-S-Pb isotopic
1139 compositions and Sm-Nd isotopic age. Journal of Asian Earth Sciences 73,

1140 39–47.
1141 Zhou, J.X., Huang, Z.L., Zhou, M.F., Li, X.B., Jin, Z.G., 2013a. Constraints of
1142 C-O-S-Pb isotope compositions and Rb-Sr isotopic age on the origin of the
1143 Tianqiao carbonate-hosted Pb-Zn deposit, SW China. Ore Geology
1144 Reviews 53, 77–92.
1145 Zhou, J.X., Huang, Z.L., Zhou, M.F., Zhu, X.K., Muchez, P., 2014a. Zinc, sulfur
1146 and lead isotopic variations in carbonate-hosted Pb-Zn sulfide deposits,
1147 southwest China. Ore Geology Reviews 58, 41–54.
1148 Zhou, J.X., Wang X.C., Wilde, S.A., Luo, K., Huang, Z.L., Wu, T., Jin, Z.G.,
1149 2018. New insights into the metallogeny of MVT Pb-Zn deposits: A case
1150 study from the Nayongzhi in South China, using field data, fluid
1151 compositions, and in situ S-Pb isotopes. American Mineralogist, in press.
1152 Doi: http://dx.doi.org/10.2138/am-2018-6238.
1153 Zhou, M.F., Yan, D.P., Kennedy, A.K., Li, Y.Q., Ding, J., 2002. SHRIMP zircon
1154 geochronological and geochemical evidence for Neo-Proterozoic arc-
1155 related magmatism along the western margin of the Yangtze Block, South
1156 China. Earth and Planetary Science Letters 196, 1–67.
1157 Zhou, M.F., Zhao, X.F., Chen, W.T., Li, X.C., Wang, W., Yan, D.Y., Qiu, H.N.,
1158 2014c. Proterozoic Fe-Cu metallogeny and supercontinental cycles of the
1159 southwestern Yangtze Block, southern China and northern Vietnam. Earth
1160 Science Review 139, 59–82.
1161 Zhu, C.W., Wen, H.J., Zhang, Y.X., Fu, S.H., Fan, H.F., Cloquet, C., 2017.

Cadmium isotope fractionation in the Fule Mississippi Valley-type deposit, Southwest China: Mineralium Deposita 52, 675–686.

Zhu, B.Q., Hu, Y.G., Zhang, Z.W., Cui, X.J., Mo, D.M., Chen, G.H., Peng, J.H., Sun, Y.G., Liu, D.H., Chang, X.Y., 2007. Geochemistry and geochronology of native copper mineralization related to the Emeishan flood basalts, Yunnan Province, China. Ore Geology Reviews 32, 366–380.

Zhu, C., Wen, H., Zhang, Y., Fan, H., 2016. Cadmium and sulfur isotopic compositions of the Tianbaoshan Zn-Pb-Cd deposit, Sichuan Province, China. Ore Geology Reviews 76, 152–162.

Figure captions

Fig. 1 a: Regional geological setting of SW China, highlighting the general study area; b: Geological sketch map of the Sichuan-Yunnan-Guizhou (SYG) Pb-Zn metallogenic province (modified from Liu and Lin, 1999), which shows the distribution of Pb-Zn deposits, native Cu deposits, strata, faults and igneous rocks.

Fig. 2 Geological sketch map of the Fule district (modified from Liu and Lin, 1999), showing the distribution of Pb-Zn deposits, strata, faults and Emeishan basalts.

Fig. 3 A-B cross-section through the Fule district (modified from Liu and Lin,

1999), revealing the distribution of ore bodies, faults and strata, and the spatial relationship between sulfide ores and basalts.

Fig. 4. Field photographs of the Fule deposit; a: F_6 reverse fault plane with chloritization; b: post-ore dolomite/calcite (Dol/Cal) veins fill fractures in dolostone; c: sphalerite (Sp) and galena (Gn) occur as massive aggregates that are filled by Dol/Cal crumbs, and carbonate breccias are cemented by Dol/Cal veins; d: Dol/Cal occur as crumbs and fill fractures in massive Sp and Gn aggregates; e: massive Sp and Gn aggregates are filled/cemented by Dol/Cal veins; f: massive Sp and Gn, and carbonate breccias are filled/cemented by Dol/Cal veins; g: breccias of sulfide ore and carbonate are cemented by Dol/Cal crumb aggregates; h: interbedded sulfide veins are filled/cemented by Dol/Cal veins or veinlets; h-n: massive Sp and Gn are filled/cemented by Dol/Cal veins; o: massive Sp and Gn; p: Dol/Cal veins fill fractures in the wall rocks or cement carbonate breccias, and Sp and Gn occur as speckles or single crystals that are irregularly distributed in the wall rocks; q-r: massive Sp and/or Gn are filled/cemented by Dol/Cal veins; t: post-ore Dol/Cal veins fill fractures in the wall rocks or cement the carbonate breccias.

Fig. 5 Photographs of hand specimens from the Fule deposit; a: dense massive sulfide ore, sphalerite (Sp) coexists with galena (Gn); b-d: interbedded sulfide veins between calcite/dolomite (Cal/Dol) millimeter-scale veinlets; e: massive

Sp and Gn are filled/cemented by Cal/Dol crumbs, veinlets or veins; f: sulfide ore breccias are cemented by Cal/Dol aggregates; g-h: Sp and Gn occur as speckles or single crystals that are either densely or sparsely distributed in dolostone, which is filled by Cal/Dol veins; i-j: Sp and Gn occur as speckles or single crystals that are distributed in Cal/Dol aggregates, which are filled by barren Cal/Dol veins; these barren veins and sulfide veins together form veined ore; k: Gn occurs as massive aggregates; l-m: massive Sp and Gn are filled by Cal/Dol fragments or veinlets; n: Cal/Dol fragments fill fractures in the massive Sp and Gn ores or host disseminated Sp; o-q: massive Sp and Gn are filled by Cal/Dol fragments or veinlets; r-t: barren Cal/Dol, speckles or single crystals of Sp and/or Gn-bearing Cal/Dol and sulfide veins form veined ore.

Fig. 6 The textural and structural features of sulfide minerals in the Fule deposit under the microscope; a: sphalerite-I (Sp-I) coexists with galena-I (Gn-I), and forms veined aggregates; calcite/dolomite-I (Cal/Dol-I) forms veined aggregates and is interbedded with sulfide veins; post-ore Cal/Dol-III fills fractures in the sulfide veins; b-c: barren Cal/Dol-II, disseminated sulfide-bearing Dol-I, and Sp-I and Gn-I veins form veined ore; d: massive Sp-II and Gn-II are filled by Cal/Dol veins; e: Sp-II occurs as euhedral to anhedral fine-grained crystals and coexist with Gn-II; f: Gn-II forms subhedral medium-grained crystals that enclose Sp-I and coexist with Sp-II; g: Sp-I forms granular crystals that are filled by Cal/Dol-II, Gn-II, and tetrahedrite (Ttr); h: granular Sp-

II coexists with granular Py-II, both of which are enclosed by Dol-II; i: Chalcopyrite (Ccp) occurs as within Sp-I; j: Sp-II forms a euhedral fine-grained crystal that is enclosed by Dol-II and Cal-II; k: anhedral Sp-I coexists with Py-I and Ttr, all of which are cemented by Cal/Dol-II; i: Gn-II forms a subhedral fine-grained crystal that encloses Sp-I and coexists with Sp-II; m: fine-grained Sp-I crystal coexists with Ttr and is enclosed by coarse-grained Gn-II crystal; n: fine-grain cataclastic Py-II crystals coexist with Cal/Dol-II, both of which fill fractures in the Sp-I; o: Sp-II forms a subhedral fine-grained crystal and is enclosed by Dol-II; p: Sp-II coexists with Gn-II and Cal/Dol-II; q: Sp-I is filled by Gn-II and Cal/Dol-II; r: Gn-II encloses Py-I and coexists with Sp-II, and Py-II replaces Ccp, all of which are filled/cemented by Cal/Dol-II; s: Ccp occurs within Sp-II that forms an embayment texture with Cal/Dol-II; t: Ccp coexists with Ttr and Sp-II, all of which are filled or enclosed by Cal/Dol-II.

Fig. 7 The texture and structure of hydrothermal minerals in the Fule deposit under the scanning electron microscope (SEM); a: Sphalerite-I (Sp-I) present as euhedral-subhedral fine- to medium-grained crystals that coexist with galena-I (GnI), all of which are filled or enclosed by dolomite-I (Dol-I) that forms a solid-solution with calcite-I (Cal-I); b: Sp-I occurs as a medium-grained crystal and forms embayment texture with Dol-I that encloses Cal-I solid-solution; c: Py-II encloses Gn-I and coexists with Sp-II, both of which form embayment texture with Cal-II; e: Py-I and Gn-I are enclosed by Dol-II that fills a fracture in

1250 the Sp-I; f: apatite is enclosed by Dol-III that fills a fracture in Gn-II; g: Gn-II and
1251 Ttr fill a fracture in Sp-I; h: Ttr occurs as a fine-grained crystal that coexists with
1252 fine-grained Sp-I, all of which are enclosed by coarse-grained Gn-II that
1253 coexists with Sp-II; i: Sp-II occurs as a euhedral fine-grained crystal that is
1254 cemented or enclosed by Dol-II; j: Gn-II encloses Ttr and coexists with Sp-II; k:
1255 solid-solution texture of Dol-II and Cal-II; l: Gn-II encloses Sp-I and coexists with
1256 Ttr and Sp-II; m: Gn-II coexists with Ttr and Dol-II, of which the latter encloses
1257 Gn-I; n: Dol-II coexists with Gn-II that encloses Py-I and Ttr; o: Ttr encloses Gn-
1258 I and coexists with Gn-II and Dol-II, of which the latter forms a solid-solution
1259 texture with Cal-II; p: Gn-II coexists with Ttr and Sp-II; q: Sp-I coexists with Gn-
1260 I and Ttr; r: Gn-II forms embayment texture with Sp-II and coexists with Ttr; s:
1261 Ttr occurs as aggregate veinlets along the rim of polydymite (Pld); millerite (Mil)
1262 occurs as a micro-vein aggregate within Pld; pentlandite (Ptl) is a euhedral fine-
1263 grained crystal within Pld; Gn-I coexists with Ptl; all of them are enclosed by
1264 Dol-II that encloses Cal-II solid-solution; t: Gn-II forms fine veinlets and fills
1265 fractures in Sp-I.
1266
1267 Fig. 8 Mineral paragenesis in the Fule Pb-Zn deposit (data are sourced from Si
1268 et al., 2006 and this paper)
1269
1270 Fig. 9 The area selected for in situ S isotope analysis that has homogeneous
1271 isotopic compositions (including ^{32}S, ^{34}S, ^{75}As and $^{63}Cu^{32}S$).

Fig. 10 Plot of $\delta^{13}C$ vs. $\delta^{18}O$; C-O isotopic data for mantle, marine carbonate rocks and sedimentary organic matters are sourced from Taylor et al. (1967), Demény et al. (1998), Veizer and Hoefs (1976) and Hoefs (2009).

Fig. 11 In situ $\delta^{34}S$ values in sphalerite and paragenetic pyrite, showing the in situ $\delta^{34}S$ values for sphalerite and pyrite crystals, and their cores and rims.

Fig. 12 a: A comparison of in situ and bulk S isotopic compositions for sulfide minerals formed at generations I and II; b: Histogram of in situ and bulk S isotopic data; c: A comparison between mantle-derived S, seawater, evaporates and data from nearby Pb-Zn deposits.

Fig. 13 Plot of $^{207}Pb/^{204}Pb$ vs. $^{206}Pb/^{204}Pb$ that shows the field of late Permian Emeishan basalts, late Ediacaran-middle Permian sedimentary rocks and Proterozoic metamorphic rocks, and the Pb evolution curves of U, O, M and L (after Zartman and Doe, 1981); Upper Crust (U), Orogen Belt (O), Mantle (M) and Lower Crust (L). Whole-rock Pb isotopic data are taken from Huang et al. (2004), Li et al. (2007), Yan et al. (2007), Zhou et al. (2013a, 2014a) and Bao et al. (2017).

Fig. 14 Plots of $^{207}Pb/^{204}Pb$ vs. $^{206}Pb/^{204}Pb$ (a) and $^{208}Pb/^{204}Pb$ vs. $^{206}Pb/^{204}Pb$

(b) that display the gradually incremental increase in Pb isotopic ratios from galena-I (early phase) to galena-II (late phase).

Fig. 15 Diagram of $\delta^{13}C$ vs. $\delta^{18}O$ for calcite precipitated by W/R interaction with different R/W ratios and temperatures (400-50°C) for either HCO_3^- or H_2CO_3 as the dominant C species (after Zheng and Hoefs, 1993), showing the position of calcite-II. Initial fluids: $\delta^{13}C$ = +2‰, $\delta^{18}O$ = +6‰. $\Delta = \delta^{i}_{rock} - \delta^{f}_{rock}$; I: $\Delta^{13}C$ = +0.2‰, $\Delta^{18}O$ = +2‰; II: $\Delta^{13}C$ = +1‰, $\Delta^{18}O$ = +6‰; III: $\Delta^{13}C$ = +2‰, $\Delta^{18}O$ = +10‰.

Fig. 16 Plots of $\delta^{13}C$ vs. $\delta^{18}O$ for calcite precipitated by CO_2 degassing with H_2CO_3 (a) or HCO_3^- (b) as the dominant C species (after Zheng, 1990), showing the position of calcite-II. The batch (solid line) and Rayleigh (dashed line) degassing precipitation models change with temperature (400-50°C) and mol fraction of C in the degassed CO_2 (0.1 to 0.4) (after Zheng, 1990). The initial $\delta^{13}C_{fluid}$ and $\delta^{18}O_{fluid}$ values were taken as +2‰ and +6‰, respectively.

Fig. 17 A sketch of the metallogenic model favoured for the carbonate-hosted Pb-Zn deposits in the ELIP; a: 263-259 Ma, the eruption of the Emeishan basalts (Shellnutt, 2014) provided fluids and elevated background geothermal gradient, which facilitated and enhanced the mobilization and extraction of ore-forming elements from Proterozoic metamorphic rocks and Paleozoic sedimentary rocks; b: 257-250 Ma, metal-bearing mantle and metamorphic

1316 fluids were driven upward along regional faults during the early Indosinian
1317 Orogeny (Carter et al., 2001; Reid et al., 2007; Hu et al., 2017); c: 250-200 (-
1318 156 Ma), the ore-forming fluids were released into structural units when the
1319 overall tectonic regime changed from compression to extension between 250-
1320 200 Ma (Carter et al., 2001; Lepvrier et al., 2008; Zhou et al., 2013b), where
1321 they were trapped by the evaporitic salt and sedimentary organic-bearing units
1322 within the platform carbonate sequence at structurally-controlled depositional
1323 sites. This process resulted in the formation of S^{2-} from multiple S reservoirs via
1324 TSR and the extraction of some metals from ore-hosting rocks through W/R
1325 interaction, which then caused the precipitation of hydrothermal minerals.

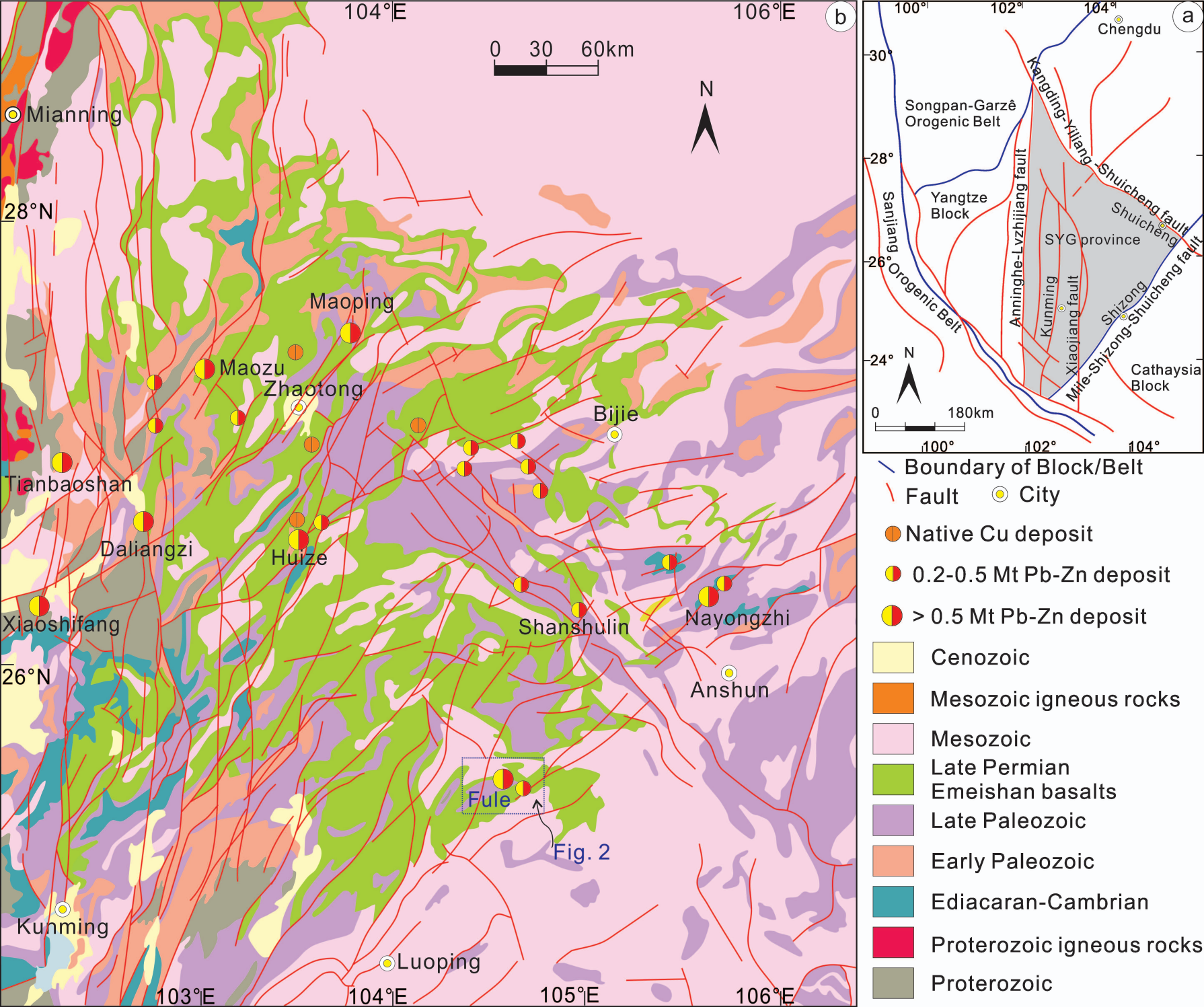
b
104°E
106°E
0 30 60km
N
Mianning
28°N
Maoping
Maozu
Zhaotong
Bijie
Tianbaoshan
Daliangzi
Huize
Xiaoshifang
26°N
Shanshulin
Nayongzhi
Anshun
Fule
Fig. 2
Kunming
Luoping
103°E
104°E
105°E
106°E
a
100°
102°
104°
Chengdu
30°
28°
26°
24°
Songpan-Garzê Orogenic Belt
Kangding-Yiliang-Shuicheng fault
Yangtze Block
Anninghe-Lvzhijiang fault
Sanjiang Orogenic Belt
SYG province
Shuicheng
Shuicheng fault
Kunming
Xiaojiang fault
Shizong
Shizong-Shuicheng fault
Mile
Cathaysia Block
N
0 180km
Boundary of Block/Belt
Fault
City
Native Cu deposit
0.2-0.5 Mt Pb-Zn deposit
> 0.5 Mt Pb-Zn deposit
Cenozoic
Mesozoic igneous rocks
Mesozoic
Late Permian Emeishan basalts
Late Paleozoic
Early Paleozoic
Ediacaran-Cambrian
Proterozoic igneous rocks
Proterozoic

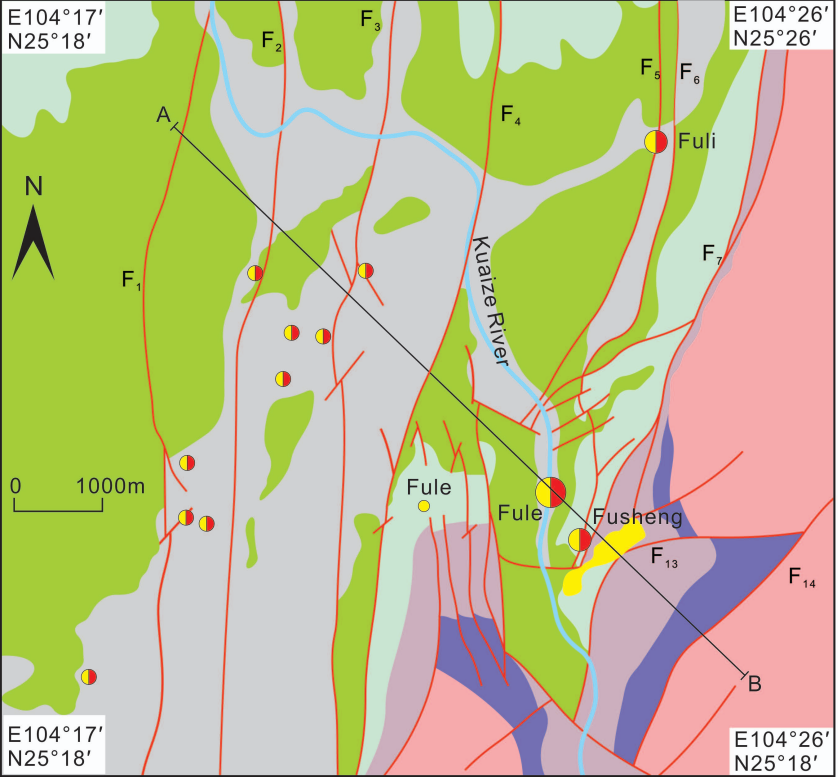

Quaternary

Middle Triassic Guanling Fm., carbonate rocks

Early Triassic Yongning-zhen Fm., carbonate rocks

Ealy Triassic Feixianguan Fm., sandstone

Late Permian Xuanwei Fm., shale

Late Permian Emeishan basalts

Middle Permian Yangxin Fm., limestone and dolostone

F_2 Fault and No.

< 0.2 Mt Pb-Zn deposit

0.2-0.5 Mt Pb-Zn deposit

> 0.5 Mt Pb-Zn deposit

A B Cross section line

Village

River

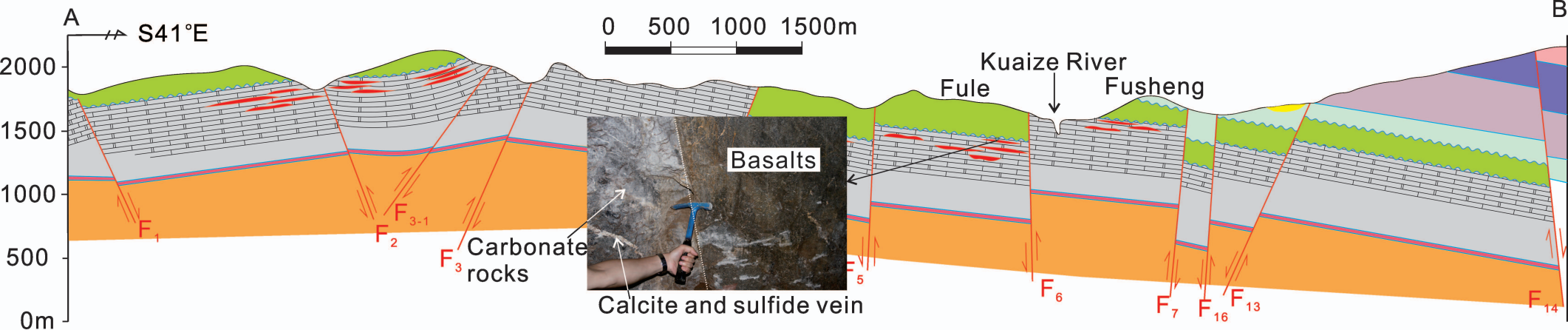
A
S41°E
0 500 1000 1500m
B
2000
1500
1000
500
0m
Kuaize River
Fule
Fusheng
Basalts
Carbonate rocks
Calcite and sulfide vein
F1
F2
F3-1
F3
F5
F6
F7
F16
F13
F14
Quaternary
Middle Triassic Guanling Fm., carbonate rocks
Early Triassic Yongningzhen Fm., carbonate rocks
Early Triassic Feixianguan Fm., sandstone
Late Permian Xuanwei Fm., shale
Late Permian Emeishan basalts
Middle Permian Yangxin Fm., limestone and dolostone
Early Permian Liangshan Fm., shale and sandstone
Late Carboniferous Maping Fm., limestone
Stratigraphic boundary
Normal fault/Reverse fault
Ore body


a
Fault plane and chloritization
F6
Limestone
b
Dolostone
Filled dol/cal vein
c
Gn
Carbonate breccia
Sp
Dolostone
Filled/cemented dol/cal crumb
d
Gn
Sp
Filled dol/cal crumb
e
Sp
Gn
Filled/cemented dol/cal vein
f
Gn
Sp
Carbonate breccia
Filled/cemented dol/cal vein
g
Carbonate breccia
Sulfide ore breccia
Sp
Gn
Cemented dol/cal crumb
h
Sp
Filled/cemented dol/cal vein
i
Sp
Gn
Filled/cemented dol/cal vein
j
Gn
Sp
Filled dol/cal vein
k
Sp
Gn
Filled dol/cal vein
l
Filled dol/cal vein
Sp
Gn
m
Filled/cemented dol/cal vein
Gn
Sp
n
Filled/cemented dol/cal vein
Gn
Sp
o
Gn
Sp
p
Filled/cemented dol/cal vein
Gn
Carbonate breccia
Sp
q
Sp
Filled/cemented dol/cal vein
r
Filled dol/cal vein
Sp
Gn
s
Gn
Sp
Filled dol/cal vein
t
Filled/cemented dol/cal vein
Carbonate breccia
Limestone


a
Sp
Gn
Dense massive sulfide ore
b
Gn
Sp
Cal/dol
Interbedded Cal/ dol and sulfide ore
c
Sp
Cal/dol
Gn
Interbedded Cal/ dol and sulfide ore
d
Interbedded Cal/ dol and sulfide ore
Sp
Gn
Cal/dol
e
Massive sulfide ore
Sp
Gn
Cal/dol
f
Brecciated ore
Cal/dol
Sp
Gn
g
Cal/dol
Gn
Sp
Dense disseminated ore
h
Cal/dol
Gn
Sp
Sparse disseminated ore
i
Ore-bearing Cal/dol
Up
Sp
Barren Cal/dol
Disseminated and veined ore
j
Sp
Cal/dol
Gn
Carbonate rocks
0.5~3cm veined ore
k
Gn
Dense massive sulfide ore
l
Cal/dol
Gn
Sp
Dense massive sulfide ore
m
Dense massive sulfide ore
Cal/dol
Gn
Sp
n
Cal/dol
Gn
Sp
Disseminated and massive ore
o
Cal/dol
Gn
Sp
Dense massive sulfide ore
p
Cal/dol
Gn
Sp
Dense massive sulfide ore
q
Dense massive sulfide ore
Cal/dol
Gn
Sp
r
Barren Cal/dol
Sp
Gn
Ore-bearing Cal/dol
Disseminated and veined ore
s
Barren Cal/dol
Sp
Gn
Ore-bearing Cal/dol
Disseminated and veined ore
t
Carbonate rocks
Cal/dol
Sp
Gn
~3cm veined ore

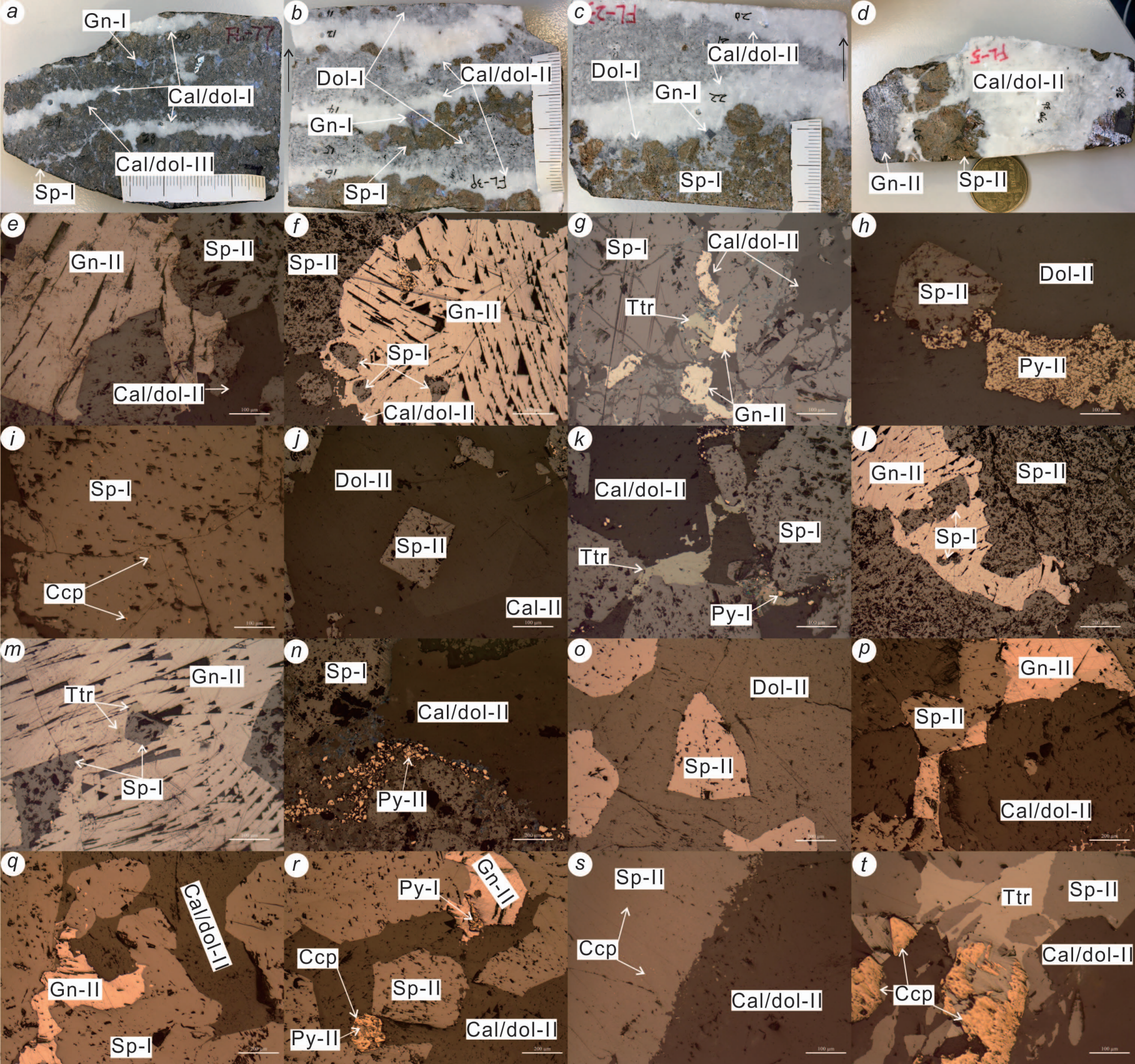
a
Gn-I
Cal/dol-I
Cal/dol-III
Sp-I
b
Dol-I
Cal/dol-II
Gn-I
Sp-I
c
Dol-I
Cal/dol-II
Gn-I
Sp-I
d
Cal/dol-II
Gn-II
Sp-II
e
Gn-II
Sp-II
Cal/dol-II
f
Sp-II
Gn-II
Sp-I
Cal/dol-II
g
Sp-I
Cal/dol-II
Ttr
Gn-II
h
Dol-II
Sp-II
Py-II
i
Sp-I
Ccp
j
Dol-II
Sp-II
Cal-II
k
Cal/dol-II
Sp-I
Ttr
Py-I
l
Gn-II
Sp-II
Sp-I
m
Ttr
Gn-II
Sp-I
n
Sp-I
Cal/dol-II
Py-II
o
Dol-II
Sp-II
p
Gn-II
Sp-II
Cal/dol-II
q
Cal/dol-II
Gn-II
Sp-I
r
Py-I
Gn-II
Ccp
Sp-II
Py-II
Cal/dol-II
s
Sp-II
Ccp
Cal/dol-II
t
Ttr
Sp-II
Cal/dol-II
Ccp

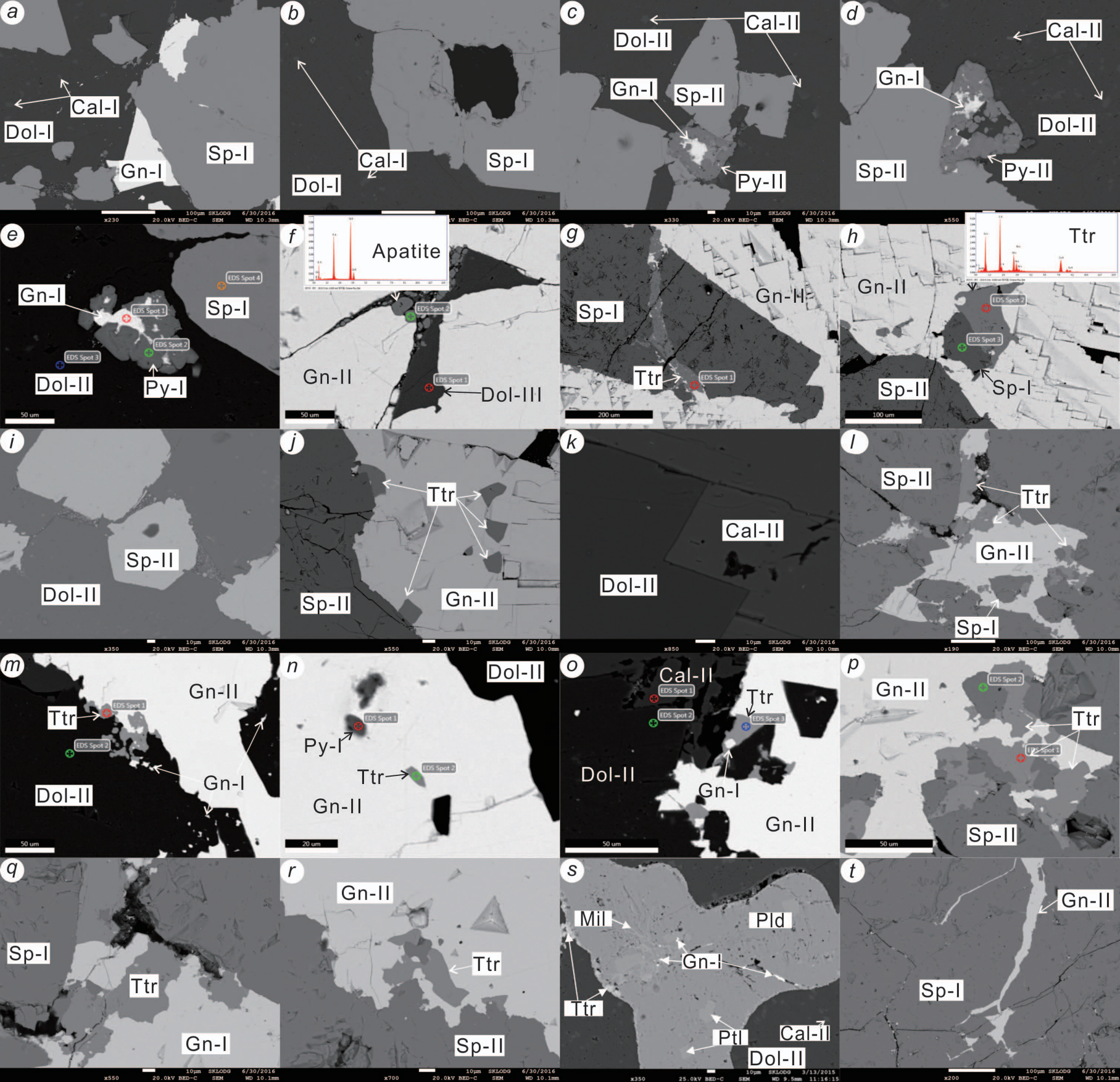
a
Cal-I
Dol-I
Sp-I
Gn-I
b
Cal-I
Dol-I
Sp-I
c
Dol-II
Cal-II
Gn-I
Sp-II
Py-II
d
Cal-II
Gn-I
Dol-II
Sp-II
Py-II
e
Gn-I
EDS Spot 4
Sp-I
EDS Spot 1
EDS Spot 2
EDS Spot 3
Dol-II
Py-I
50 um
f
Apatite
EDS Spot 2
Gn-II
EDS Spot 1
Dol-III
50 um
g
Sp-I
Gn-II
Ttr
EDS Spot 1
200 um
h
Ttr
Gn-II
EDS Spot 2
EDS Spot 3
Sp-II
Sp-I
100 um
i
Sp-II
Dol-II
j
Ttr
Sp-II
Gn-II
k
Cal-II
Dol-II
l
Sp-II
Ttr
Gn-II
Sp-I
m
Gn-II
Ttr
EDS Spot 1
EDS Spot 2
Gn-I
Dol-II
50 um
n
Dol-II
EDS Spot 1
Py-I
Ttr
EDS Spot 2
Gn-II
20 um
o
Cal-II
EDS Spot 1
EDS Spot 2
Ttr
EDS Spot 3
Dol-II
Gn-I
Gn-II
50 um
p
Gn-II
EDS Spot 2
Ttr
EDS Spot 1
Sp-II
50 um
q
Sp-I
Ttr
Gn-I
r
Gn-II
Ttr
Sp-II
s
Mil
Pld
Gn-I
Ttr
Ptl
Cal-II
Dol-II
t
Gn-II
Sp-I

Period	Diagenesis	Hydrothermal			Supergene
Stage		Sulfide + carbonate		Carbonate	Oxidized and leached
Mineral assemblage	Py + Dol	Sp + Gn + (Py + Ccp + Ttr + Pld + Ptl+ Mil) + Dol + Cal		Dol + Cal	
Generation		I	II	III	

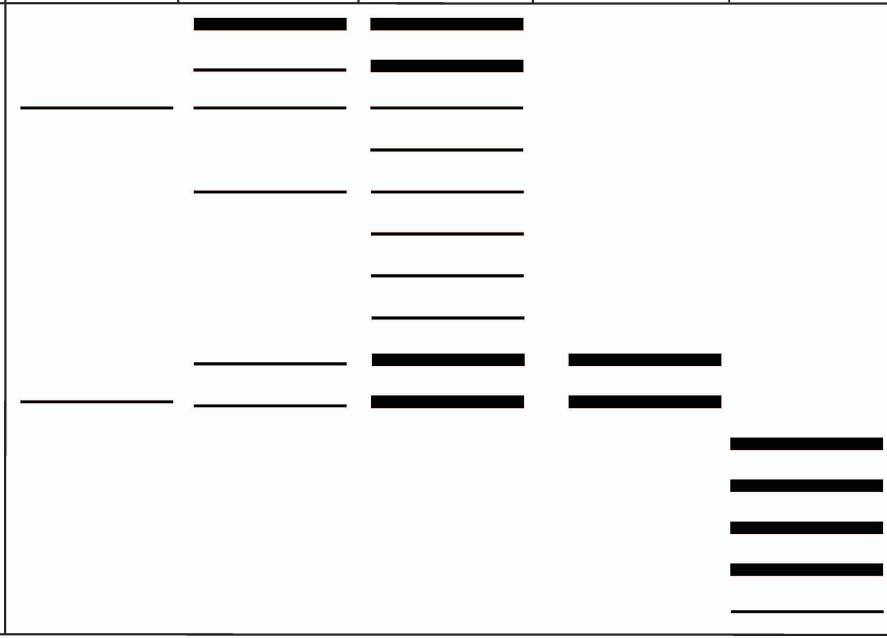

— Less; ▬ More.

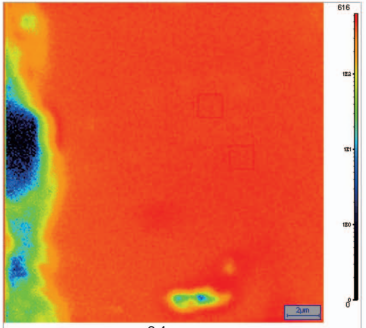

^{34}S

1/1 EM2

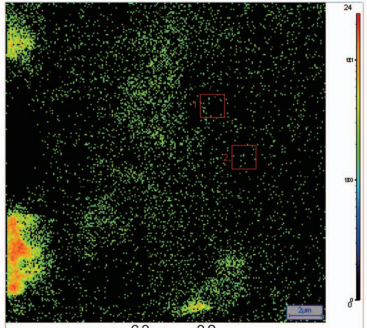

$^{63}Cu^{32}S$

1/1 EM5

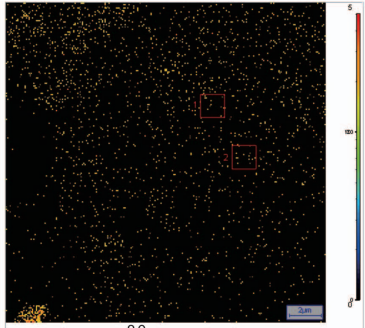

^{80}Se

1/1 EM4

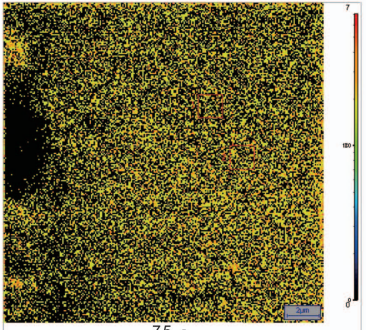

^{75}As

1/1 EM3

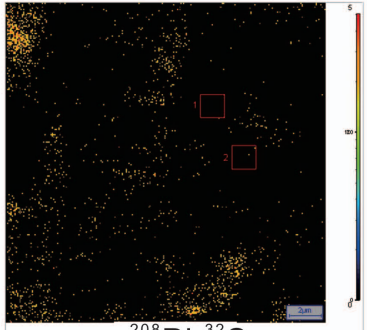

$^{208}Pb^{32}S$

1/1 EM7

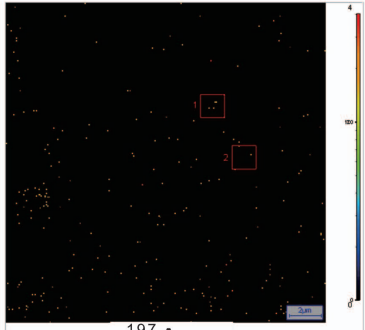

^{197}Au

1/1 EM6

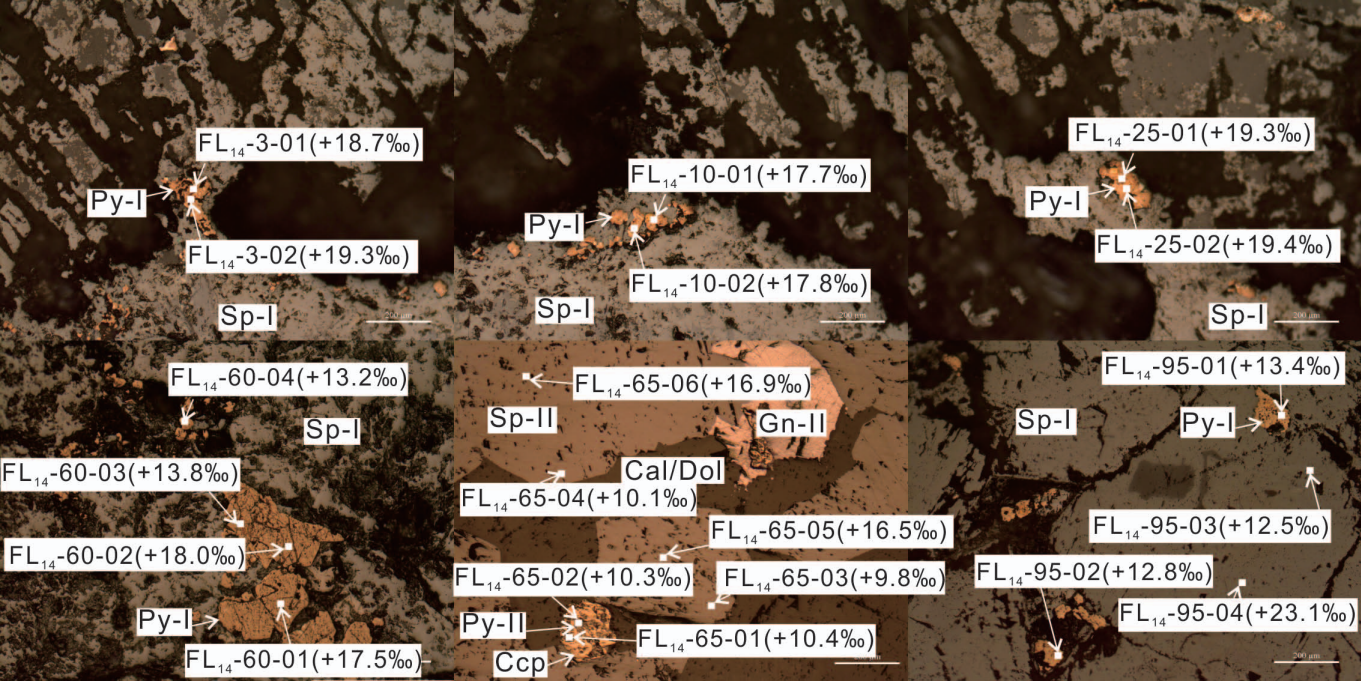
FL14-3-01(+18.7‰)
Py-I
FL14-3-02(+19.3‰)
Sp-I
FL14-10-01(+17.7‰)
Py-I
FL14-10-02(+17.8‰)
Sp-I
FL14-25-01(+19.3‰)
Py-I
FL14-25-02(+19.4‰)
Sp-I
FL14-60-04(+13.2‰)
Sp-I
FL14-60-03(+13.8‰)
FL14-60-02(+18.0‰)
Py-I
FL14-60-01(+17.5‰)
Sp-II
FL14-65-06(+16.9‰)
Gn-II
Cal/Dol
FL14-65-04(+10.1‰)
FL14-65-05(+16.5‰)
FL14-65-02(+10.3‰)
FL14-65-03(+9.8‰)
Py-II
FL14-65-01(+10.4‰)
Ccp
Sp-I
FL14-95-01(+13.4‰)
Py-I
FL14-95-03(+12.5‰)
FL14-95-02(+12.8‰)
FL14-95-04(+23.1‰)

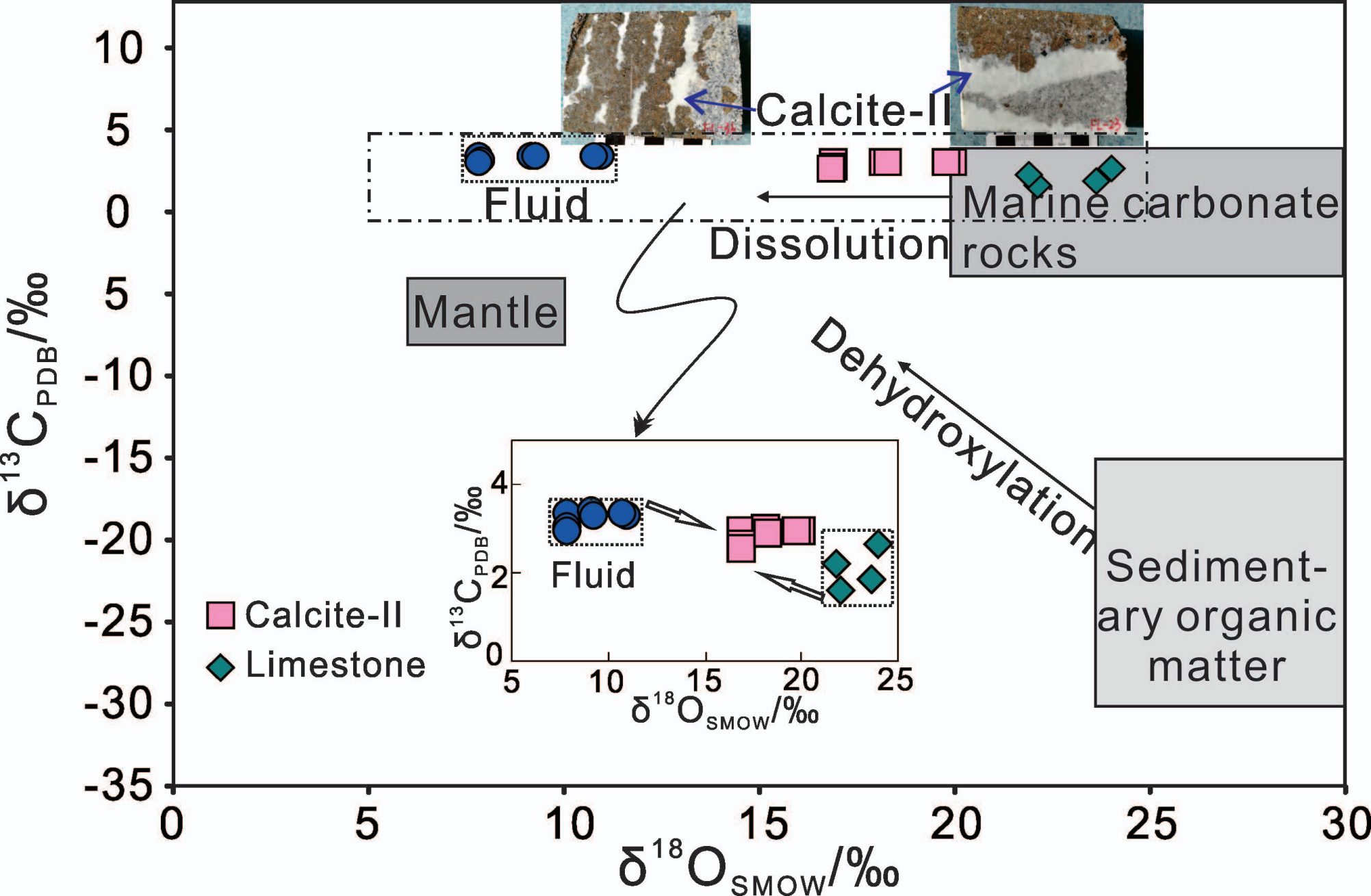
Calcite-II
Fluid
Marine carbonate rocks
Dissolution
Mantle
Dehydroxylation
Sedimentary organic matter
Calcite-II
Limestone
Fluid
δ13CPDB/‰
δ18OSMOW/‰
10
5
0
-5
-10
-15
-20
-25
-30
-35
0
5
10
15
20
25
30
4
2
0
5
10
15
20
25

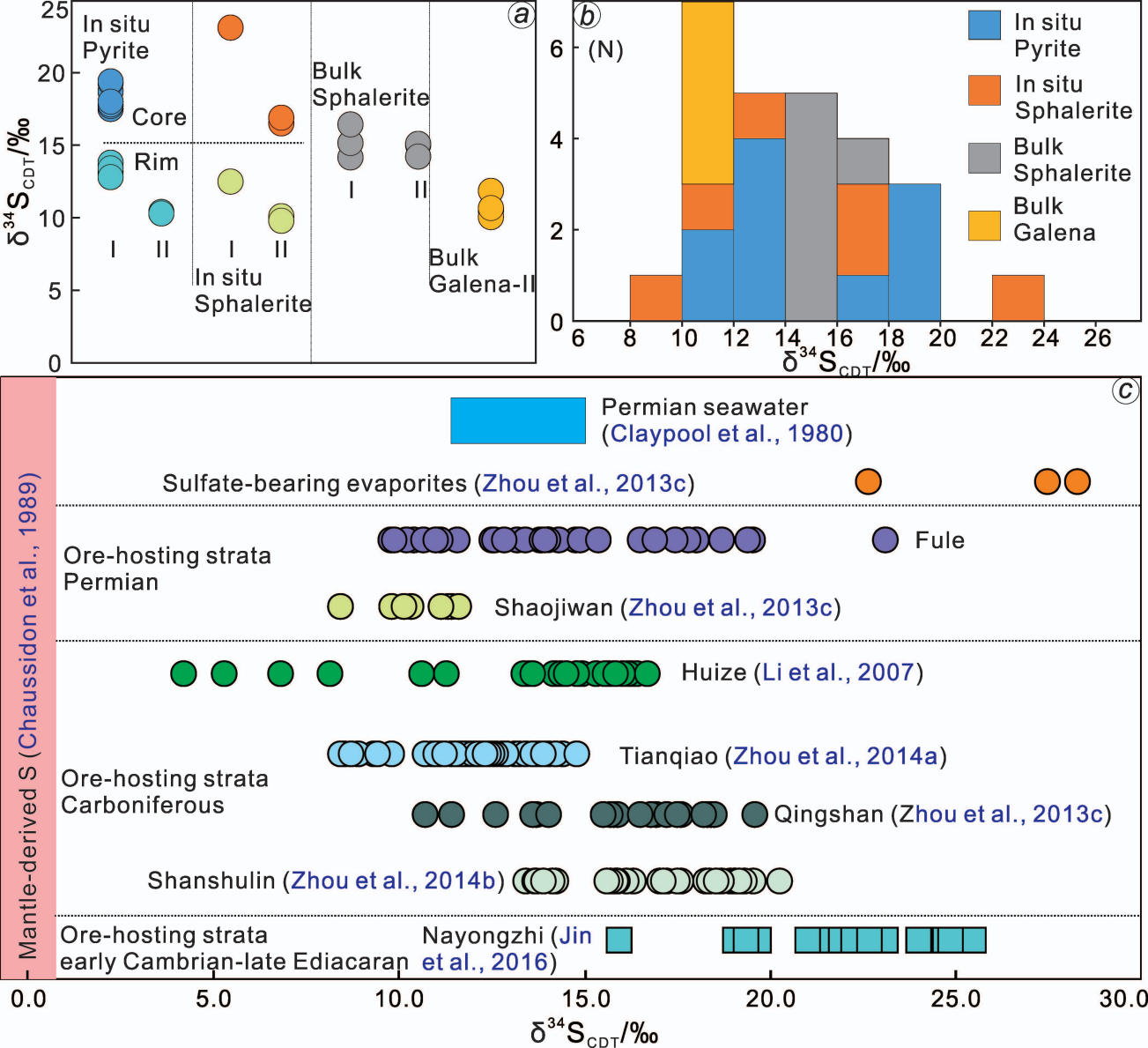
a
In situ Pyrite
Core
Rim
I
II
In situ Sphalerite
I
II
Bulk Sphalerite
I
II
Bulk Galena-II
δ34SCDT/‰
b
(N)
In situ Pyrite
In situ Sphalerite
Bulk Sphalerite
Bulk Galena
δ34SCDT/‰
c
Permian seawater (Claypool et al., 1980)
Sulfate-bearing evaporites (Zhou et al., 2013c)
Ore-hosting strata Permian
Fule
Shaojiwan (Zhou et al., 2013c)
Huize (Li et al., 2007)
Tianqiao (Zhou et al., 2014a)
Ore-hosting strata Carboniferous
Qingshan (Zhou et al., 2013c)
Shanshulin (Zhou et al., 2014b)
Ore-hosting strata early Cambrian-late Ediacaran
Nayongzhi (Jin et al., 2016)
Mantle-derived S (Chaussidon et al., 1989)
δ34SCDT/‰

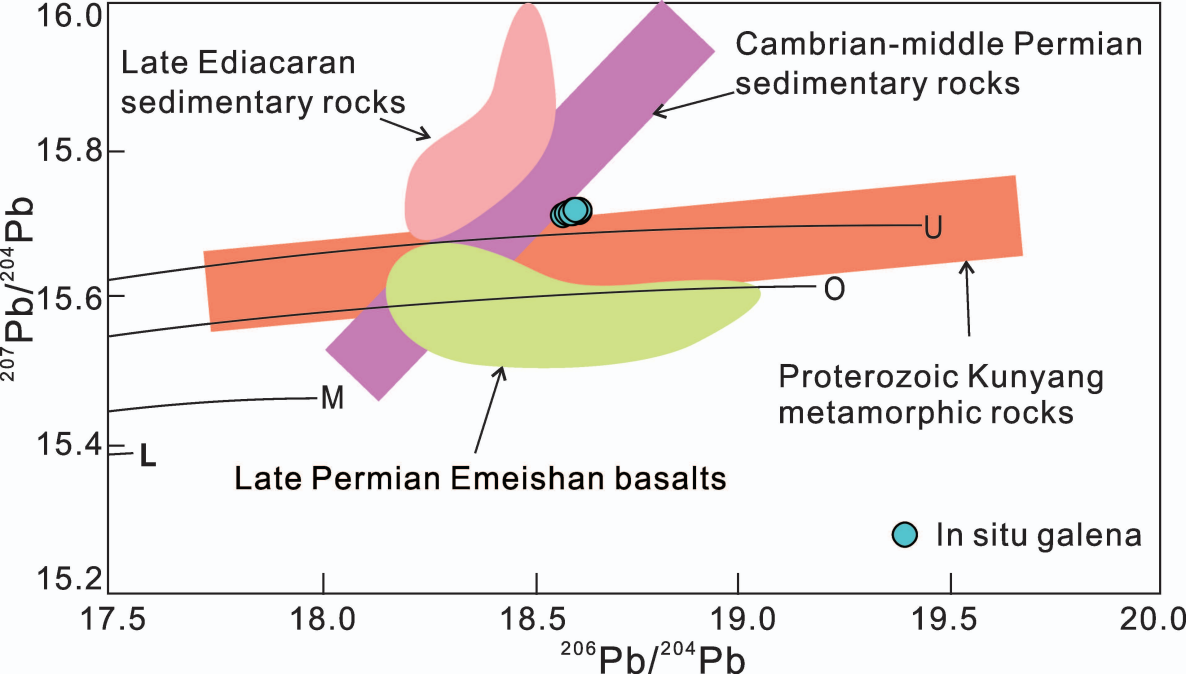
Late Ediacaran
sedimentary rocks
Cambrian-middle Permian
sedimentary rocks
U
O
M
L
Proterozoic Kunyang
metamorphic rocks
Late Permian Emeishan basalts
In situ galena
16.0
15.8
15.6
15.4
15.2
17.5
18.0
18.5
19.0
19.5
20.0
$^{207}Pb/^{204}Pb$
$^{206}Pb/^{204}Pb$

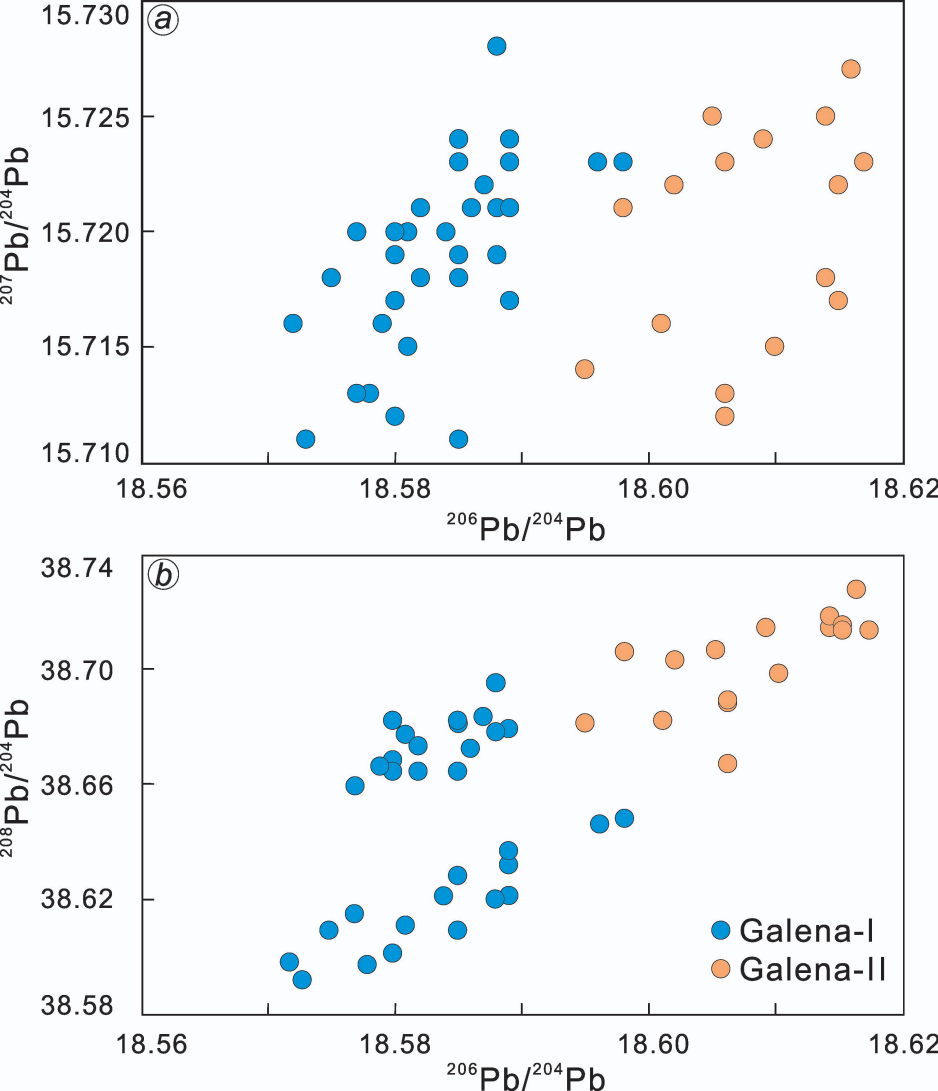
a
15.730
15.725
15.720
15.715
15.710
$^{207}Pb/^{204}Pb$
18.56
18.58
18.60
18.62
$^{206}Pb/^{204}Pb$
b
38.74
38.70
38.66
38.62
38.58
$^{208}Pb/^{204}Pb$
Galena-I
Galena-II
18.56
18.58
18.60
18.62
$^{206}Pb/^{204}Pb$

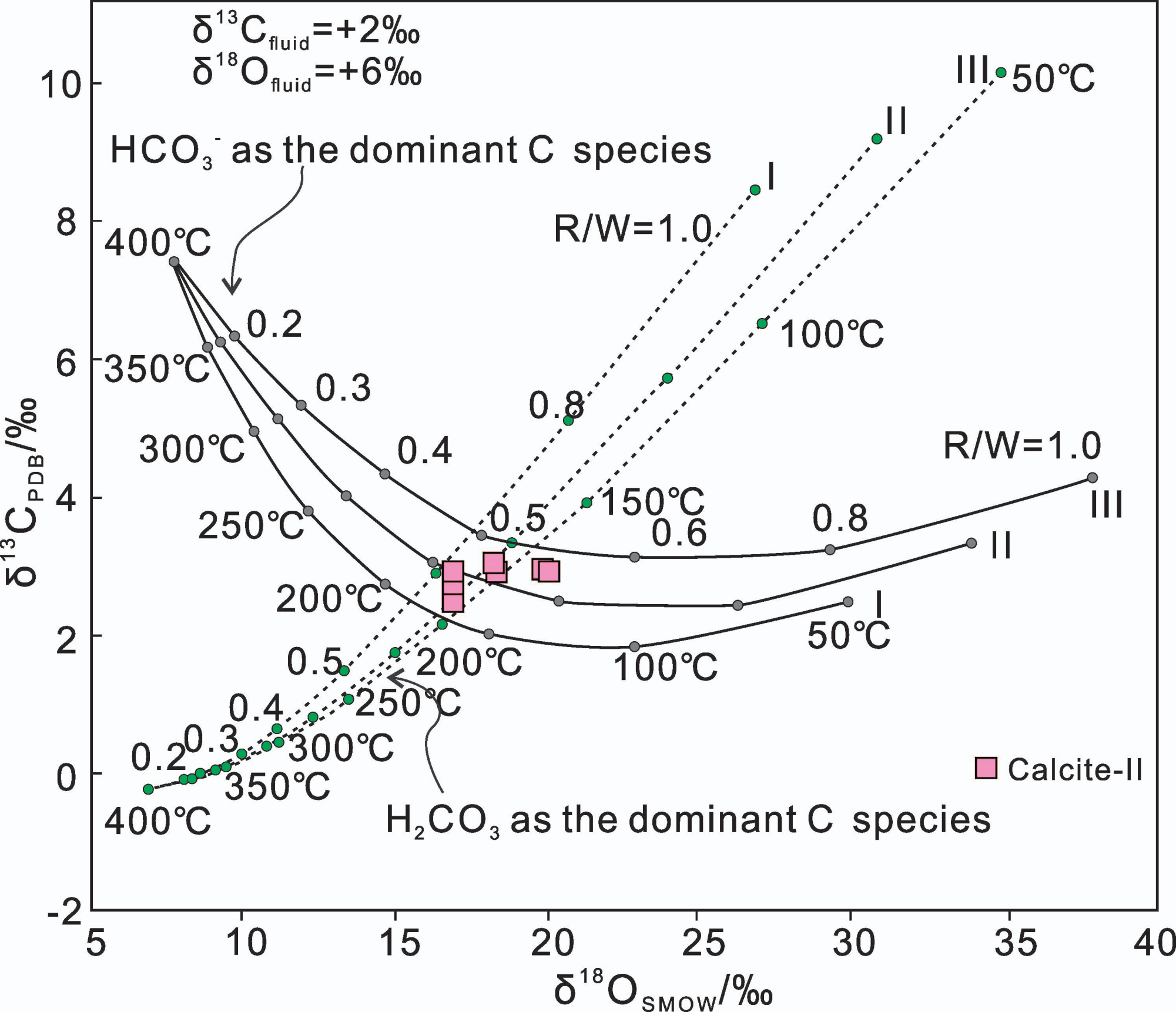
δ13Cfluid=+2‰
δ18Ofluid=+6‰
HCO3- as the dominant C species
H2CO3 as the dominant C species
400℃
350℃
300℃
250℃
200℃
150℃
100℃
50℃
0.2
0.3
0.4
0.5
0.6
0.8
R/W=1.0
I
II
III
Calcite-II
δ13CPDB/‰
δ18OSMOW/‰
10
8
6
4
2
0
-2
5
10
15
20
25
30
35
40

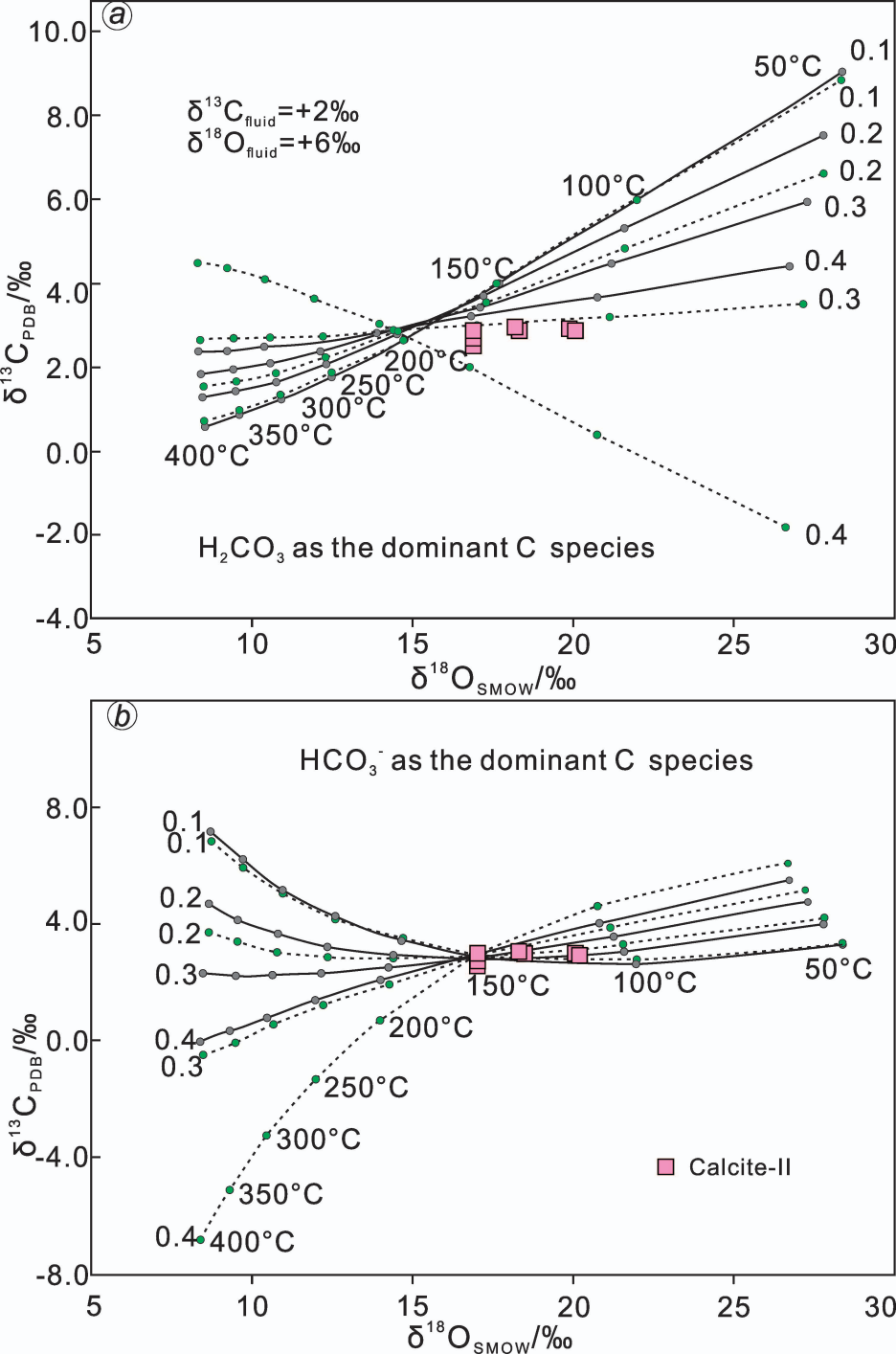
a
δ13Cfluid=+2‰
δ18Ofluid=+6‰
50°C
100°C
150°C
200°C
250°C
300°C
350°C
400°C
0.1
0.1
0.2
0.2
0.3
0.4
0.3
0.4
H2CO3 as the dominant C species
δ13CPDB/‰
δ18OSMOW/‰
b
HCO3- as the dominant C species
Calcite-II

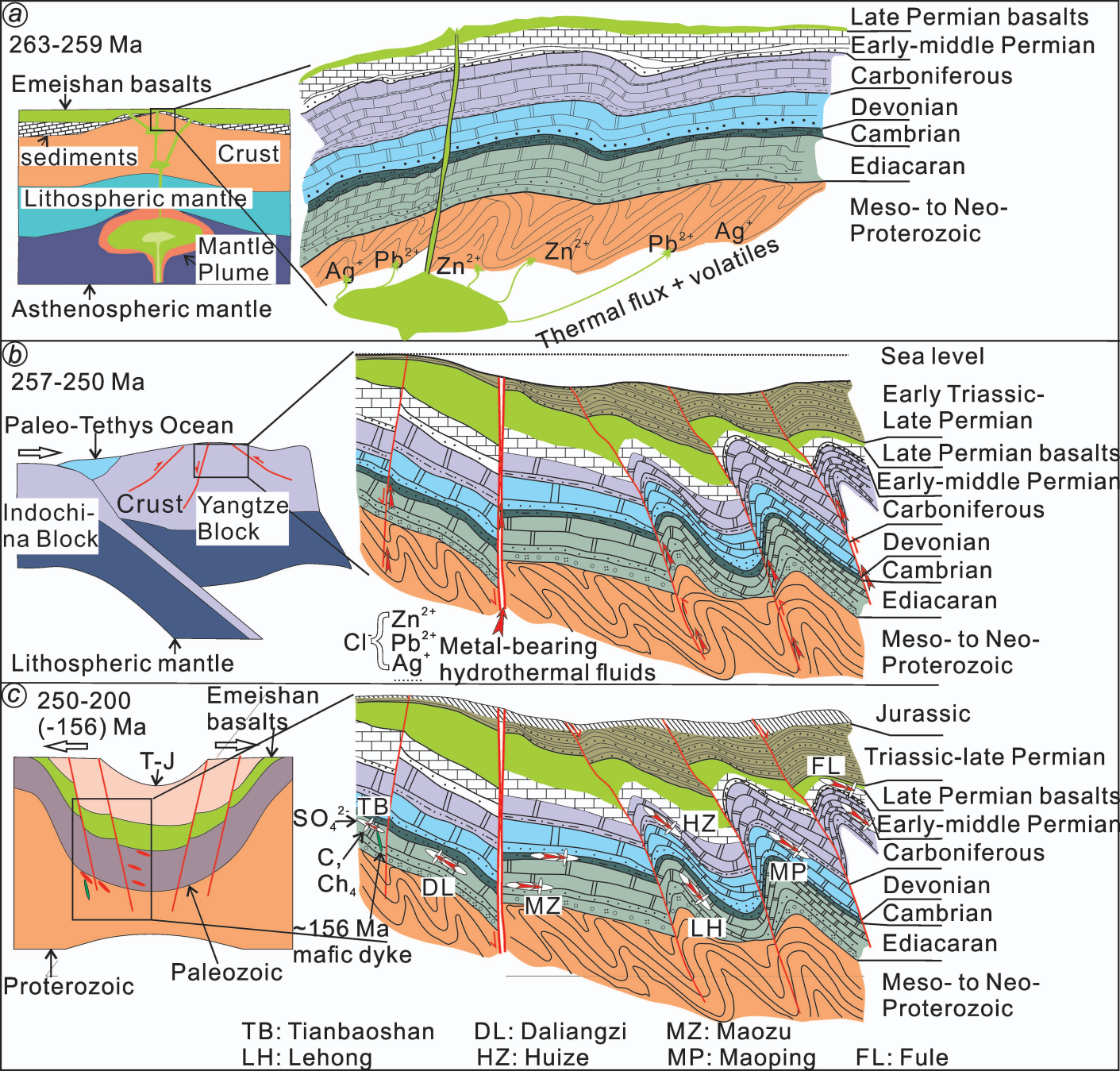
a
263-259 Ma
Emeishan basalts
sediments
Crust
Lithospheric mantle
Mantle Plume
Asthenospheric mantle
Late Permian basalts
Early-middle Permian
Carboniferous
Devonian
Cambrian
Ediacaran
Meso- to Neo-Proterozoic
Ag+ Pb2+ Zn2+ Zn2+ Pb2+ Ag+
Thermal flux + volatiles
b
257-250 Ma
Paleo-Tethys Ocean
Indochi-na Block
Crust
Yangtze Block
Lithospheric mantle
Sea level
Early Triassic-Late Permian
Late Permian basalts
Early-middle Permian
Carboniferous
Devonian
Cambrian
Ediacaran
Meso- to Neo-Proterozoic
Cl- Zn2+ Pb2+ Ag+ Metal-bearing hydrothermal fluids
c
250-200 (-156) Ma
Emeishan basalts
T-J
Proterozoic
Paleozoic
SO4 2- TB
C, Ch4
DL
MZ
~156 Ma mafic dyke
HZ
MP
LH
FL
Jurassic
Triassic-late Permian
Late Permian basalts
Early-middle Permian
Carboniferous
Devonian
Cambrian
Ediacaran
Meso- to Neo-Proterozoic
TB: Tianbaoshan
DL: Daliangzi
MZ: Maozu
LH: Lehong
HZ: Huize
MP: Maoping
FL: Fule

Table 1

C-O isotopic compositions of calcite and limestone in the Fule deposit

No.	Locations	Mineral	$\delta^{13}C_{PDB}$/‰	$\delta^{18}O_{SMOW}$/‰	$\delta^{13}C_{CO2}$/‰[a]	$\delta^{18}O_{H2O}$/‰[b]
FL_{14}-2	Nos.108, 904 and 74 ore bodies	Calcite-II	+2.94	+16.84	+3.33	+7.81
FL_{14}-23		Calcite-II	+2.93	+19.92	+3.32	+10.89
FL_{14}-44		Calcite-II	+3.01	+18.15	+3.40	+9.12
FL_{14}-64		Calcite-II	+2.96	+19.77	+3.35	+10.74
FL_{14}-8		Calcite-II	+2.67	+16.86	+3.06	+7.83
FL_{14}-68		Calcite-II	+2.57	+16.83	+2.96	+7.80
FL_{14}-36		Calcite-II	+2.92	+18.25	+3.31	+9.22
FL_{14}-D1	The mining area periphery	Limestone	+1.85	+23.61		
FL_{14}-D2		Limestone	+1.58	+22.08		
FL_{14}-D3		Limestone	+2.18	+21.85		
FL_{14}-D4		Limestone	+2.63	+24.01		

[a] $1000\ln\alpha_{(CO_2 - Calcite)} = -2.4612 + 7.663 \times 10^3 / (t + 273.15) - 2.988 \times 10^6 / (t + 273.15)^2$ (Bottinga, 1968);

[b] $1000\ln\alpha_{(Calcite - H_2O)} = 2.78 \times 10^6 / (t + 273.15)^2 - 3.39$ (O'Neil et al., 1969)

t = 180-210 °C (average 200 °C), based on temperature analysis of fluid inclusion in sphalerite-II (Li ZL unpublished data).

Table 2

In situ and bulk S isotopic compositions of sulfide minerals in the Fule deposit

No.	Locations	Mineral	$\delta^{34}S_{CDT}$/‰	Method
FL_{14}-3-01	Core	Pyrite-I	+18.7	
FL_{14}-3-02	Core	Pyrite-I	+19.3	
FL_{14}-10-01	Core	Pyrite-I	+17.7	
FL_{14}-10-02	Core	Pyrite-I	+17.8	
FL_{14}-25-01	Core	Pyrite-I	+19.3	
FL_{14}-25-02	Core	Pyrite-I	+19.4	
FL_{14}-60-01	Core	Pyrite-I	+17.5	
FL_{14}-60-02	Core	Pyrite-I	+18.0	
FL_{14}-60-03	Rim	Pyrite-I	+13.8	
FL_{14}-60-04	Rim	Pyrite-I	+13.2	In situ
FL_{14}-65-01	Rim	Pyrite-II	+10.4	analysis
FL_{14}-65-02	Rim	Pyrite-II	+10.3	
FL_{14}-65-03	Rim	Sphalerite-II	+9.8	
FL_{14}-65-04	Rim	Sphalerite-II	+10.1	
FL_{14}-65-05	Core	Sphalerite-II	+16.5	
FL_{14}-65-06	Core	Sphalerite-II	+16.9	
FL_{14}-95-01	Rim	Pyrite-I	+13.4	
FL_{14}-95-02	Rim	Pyrite-I	+12.8	
FL_{14}-95-03	Rim	Sphalerite-I	+12.5	
FL_{14}-95-04	Core	Sphalerite-I	+23.1	
FL_{14}-13		Galena-II	+11.86	
FL_{14}-24		Galena-II	+10.49	
FL_{14}-58		Galena-II	+10.04	
FL_{14}-75		Galena-II	+10.66	
FLC-0-1		Sphalerite-II	+15.02	Bulk
FLC-0-3		Sphalerite-II	+15.10	analysis
FLC-0-5		Sphalerite-II	+14.21	
FLC-0-8		Sphalerite-I	+14.16	
FLC-0-9		Sphalerite-I	+15.16	
FLC-0-16		Sphalerite-I	+16.43	

Table 3

In situ Pb isotopic compositions of galena in the Fule deposit

No.	Mineral	$^{206}Pb/^{204}Pb$	1s	$^{207}Pb/^{204}Pb$	1s	$^{208}Pb/^{204}Pb$	1s
FL_{14}-17-01	Galena-I	18.588	0.003	15.721	0.003	38.678	0.01
FL_{14}-17-02	Galena-I	18.589	0.003	15.724	0.003	38.679	0.007
FL_{14}-17-03	Galena-I	18.585	0.002	15.718	0.002	38.664	0.007
FL_{14}-17-04	Galena-I	18.580	0.002	15.717	0.002	38.664	0.006
FL_{14}-17-05	Galena-I	18.577	0.002	15.713	0.002	38.659	0.008
FL_{14}-17-06	Galena-I	18.581	0.003	15.720	0.003	38.677	0.008
FL_{14}-17-07	Galena-I	18.585	0.002	15.723	0.002	38.682	0.005
FL_{14}-17-08	Galena-I	18.586	0.002	15.721	0.002	38.672	0.006
FL_{14}-25-01	Galena-I	18.582	0.002	15.718	0.002	38.664	0.005
FL_{14}-25-02	Galena-I	18.585	0.002	15.724	0.002	38.681	0.005
FL_{14}-25-03	Galena-I	18.580	0.002	15.719	0.002	38.668	0.005
FL_{14}-25-04	Galena-I	18.582	0.002	15.721	0.002	38.673	0.006
FL_{14}-25-05	Galena-I	18.580	0.002	15.720	0.002	38.682	0.006
FL_{14}-25-06	Galena-I	18.579	0.002	15.716	0.002	38.666	0.007
FL_{14}-25-07	Galena-I	18.588	0.003	15.728	0.003	38.695	0.009
FL_{14}-25-08	Galena-I	18.587	0.002	15.722	0.002	38.683	0.007
FL_{14}-40-01	Galena-I	18.581	0.003	15.715	0.003	38.611	0.008
FL_{14}-40-02	Galena-I	18.584	0.003	15.720	0.003	38.621	0.007
FL_{14}-40-03	Galena-I	18.589	0.002	15.723	0.002	38.637	0.007
FL_{14}-40-04	Galena-I	18.585	0.002	15.719	0.002	38.628	0.006
FL_{14}-40-05	Galena-I	18.573	0.002	15.711	0.002	38.592	0.006
FL_{14}-40-06	Galena-I	18.577	0.003	15.720	0.003	38.615	0.007
FL_{14}-40-07	Galena-I	18.589	0.002	15.721	0.002	38.632	0.006
FL_{14}-40-08	Galena-I	18.596	0.002	15.723	0.003	38.646	0.007
FL_{14}-59-01	Galena-I	18.598	0.002	15.723	0.003	38.648	0.007
FL_{14}-59-02	Galena-I	18.585	0.002	15.711	0.002	38.609	0.007
FL_{14}-59-03	Galena-I	18.589	0.002	15.717	0.002	38.621	0.006
FL_{14}-59-04	Galena-I	18.588	0.002	15.719	0.002	38.620	0.006
FL_{14}-59-05	Galena-I	18.575	0.002	15.718	0.002	38.609	0.005
FL_{14}-59-06	Galena-I	18.572	0.002	15.716	0.002	38.598	0.006
FL_{14}-59-07	Galena-I	18.578	0.003	15.713	0.003	38.597	0.008
FL_{14}-59-08	Galena-I	18.580	0.002	15.712	0.002	38.601	0.006
FL_{14}-75-01	Galena-II	18.606	0.003	15.723	0.003	38.667	0.008
FL_{14}-75-02	Galena-II	18.614	0.002	15.718	0.002	38.718	0.007
FL_{14}-75-03	Galena-II	18.615	0.002	15.717	0.002	38.713	0.006
FL_{14}-75-04	Galena-II	18.610	0.002	15.715	0.002	38.698	0.006
FL_{14}-75-05	Galena-II	18.615	0.002	15.722	0.002	38.715	0.006
FL_{14}-75-06	Galena-II	18.616	0.002	15.727	0.002	38.727	0.006
FL_{14}-75-07	Galena-II	18.609	0.003	15.724	0.003	38.714	0.007
FL_{14}-75-08	Galena-II	18.606	0.002	15.713	0.002	38.689	0.006

FL_{14}-95-01	Galena-II	18.606	0.002	15.712	0.002	38.688	0.006
FL_{14}-95-02	Galena-II	18.617	0.002	15.723	0.002	38.713	0.007
FL_{14}-95-03	Galena-II	18.614	0.002	15.725	0.002	38.714	0.005
FL_{14}-95-04	Galena-II	18.602	0.002	15.722	0.002	38.703	0.005
FL_{14}-95-05	Galena-II	18.598	0.002	15.721	0.002	38.706	0.006
FL_{14}-95-06	Galena-II	18.605	0.002	15.725	0.002	38.706	0.006
FL_{14}-95-07	Galena-II	18.601	0.002	15.716	0.002	38.682	0.007
FL_{14}-95-08	Galena-II	18.595	0.002	15.714	0.002	38.681	0.006

Table 4

A comparison between the Fule, Huize and typical MVT deposits

Characteristics	Huize (typical SYG-type)	MVT	Fule
Grade	Pb + Zn: 25-35 wt. %, Zn/(Zn + Pb): 0.9±	Pb + Zn: av. <10 wt. %, Zn/(Zn + Pb): 0.8±	Pb + Zn: av. 15-20 wt. %, Zn/(Zn + Pb): 0.9±
Tonnage	Pb + Zn metal reserves: single ore body ~1 Mt, total > 7 Mt	Pb + Zn metal reserves: single ore body < 1 Mt	Pb + Zn metal reserves: single ore body ~0.5 Mt, total > 1 Mt
Acreage	The SYG province covers 170, 000 km^2	Hundreds of square kilometers	The SYG province covers 170, 000 km^2
Host rocks	Early Carboniferous coarse-grained dolostone	Cambrian to Carboniferous carbonate rocks	Middle Permian dolostone
Depth of Mineralization	>2000 m	<1500 m	<400 m
Tectonic setting	Western Yangtze Block, controlled by NE reverse fault-fold tectonic system	Typically located within extensional zones inboard of orogenic belts	Western Yangtze Block, controlled by NE reverse fault-fold tectonic system
Relation with magmatic activity	Genetically associated with late Permian Emeishan basalts	Generally has no genetic association with magmatic activity	Genetically associated with late Permian Emeishan basalts
Ore-controlled factors	Controlled by thrust fault-fold structure and lithology	Mainly controlled by structure and lithology	Controlled by fault-fold structure and lithology
Age	~225 Ma	From Proterozoic to Cretaceous	250-200 Ma
Ore texture and structure	Mainly exhibiting massive structures, and fine-, medium- and coarse-grained textures	Exhibiting disseminated, fine granular, branched, colloidal and massive structures and colloidal, skeleton coarse-crystalline textures	Mainly exhibiting massive structures, and fine-, medium- and coarse-grained textures
Mineral compositions	Sphalerite, galena, pyrite and calcite	Sphalerite, galena, pyrite, barite, fluorite, calcite and dolomite.	Sphalerite, galena, pyrite, chalcopyrite, tetrahedrite, millerite, polydymite, pentlandite, calcite and dolomite
Fluid inclusions	<10 wt. % NaCl equiv.; Cl^{-}-Na^{+}-Ca^{2+}-Mg^{2+}-SO_4^{2-}; 150-300°C	10-30wt. % NaCl equiv.; Cl^{-}-Na^{+}-Ca^{2+}-K^{+}-Mg^{2+}; 50-200°C	4-10 wt. % NaCl equiv.; Cl^{-}-Na^{+}-Ca^{2+}-Mg^{2+}-SO_4^{2-}; 120-260°C
Associated metals	Ag, Cu, Ge, Ga, Cd and In	Ag	Ag, Cu, Ni, Cd, Ge, Ga and In
O isotopes	Generated from W/R interaction between mantle/metamorphic fluids and carbonate rocks	Sourced from carbonate rocks	Generated from W/R interaction between /metamorphic fluids and carbonate rocks
S isotopes	+11-+17‰, sourced from multiple S reservoirs	+10-+25‰, sourced from evaporates within sedimentary strata	+9-+23‰, sourced from multiple S reservoirs
Pb isotopes	Normal and uniform Pb isotopes, sourced from a well-mixed source	Complicated Pb isotopic ratios and regional zonation	Normal and uniform Pb isotopes, sourced from a well-mixed source
Precipitation of sulfide	Fluid mixing + sulfate reduction	Reduced S, local sulfate reduction, or metal and reduced S-mixing	Fluid mixing + sulfate reduction
Tectonic setting	Changed from compression to extension	Extensional basin	Changed from compression to extension
References	Zhou et al., 2001; Li et al., 2007; Huang et al., 2010	Leach et al., 2005, 2010	Zhu et al., 2017; This paper